Check for updates

JGR Atmospheres

RESEARCH ARTICLE
10.1029/2022JD037395

Impact of Wildfires on Mineral Dust Emissions in Europe

Laurent Menut[1], Guillaume Siour[2], Bertrand Bessagnet[3], Arineh Cholakian[1], Romain Pennel[1], and Sylvain Mailler[1]

[1]Laboratoire de Météorologie Dynamique (LMD), Ecole Polytechnique, Ecole des Ponts, Marne-la-Vallée, CNRS, IPSL Research University, Ecole Normale Supérieure, Université Paris-Saclay, Sorbonne Universités, UPMC Université Paris 06, Palaiseau, France, [2]CNRS, LISA, Université Paris Est Créteil, Université Paris Cité, Créteil, France, [3]Joint Research Centre, European Commission, Ispra, Italy

Abstract Mineral dust emissions mainly depend on soil erodibility and near-surface wind speeds. During biomass burning episodes, pyroconvection locally generates high surface wind speed and non-desert surfaces (such as forest and shrubs) are partially replaced by barren soil. These effects may induce additional mineral dust emission. However, they are generally not taken into account in chemistry-transport models since the biomass burning and mineral dust emissions are usually considered as independent processes. This may lead to an underestimation of the mineral dust emissions and therefore of the transported concentrations. In this study, this link is added in the CHIMERE chemistry-transport model. The summer of 2021 is modeled over Europe using the coupled WRF-CHIMERE system. Simulations with and without the link between emission processes are performed. Results are compared to observations such as surface measurements of ozone and particulate matter by EEA and aerosol optical depth by AERONET. With more emitted mineral dust, an effect is found on the whole meteorological and chemical system: wind, temperature, cloud, gas (such as ozone with a few ppb changes) and aerosol concentrations are changed. The effect does not appear to be very important but significant enough to have to be taken into account in future modeling.

Plain Language Summary Biomass burning inject pollutants into the atmosphere but also change meteorological and surface characteristics. During the fire, forced convection can drive mineral aerosols aloft. After the fire, the burned surface becomes more erodible. To account for these interactions between fire and mineral dust emissions, we have developed a new parameterization in the coupled WRF-CHIMERE model. We quantify the impact of this interaction and show the regions in Europe where it adds erodible surfaces.

Key Points:

- Wildfires emissions create erodible surfaces and enhanced mineral dust emissions
- Additional mineral dust emissions are modeled over western Europe with the WRF-CHIMERE online regional modeling
- The impact of these additional emission have an impact on meteorology and other gas and aerosol concentrations via the direct and indirect aerosol effect

Correspondence to:
L. Menut,
laurent.menut@lmd.ipsl.fr

Citation:
Menut, L., Siour, G., Bessagnet, B., Cholakian, A., Pennel, R., & Mailler, S. (2022). Impact of wildfires on mineral dust emissions in Europe. *Journal of Geophysical Research: Atmospheres*, *127*, e2022JD037395. https://doi.org/10.1029/2022JD037395

Received 27 JUN 2022
Accepted 5 DEC 2022

Author Contributions:
Conceptualization: Laurent Menut
Methodology: Laurent Menut
Software: Laurent Menut, Guillaume Siour, Bertrand Bessagnet, Arineh Cholakian, Romain Pennel, Sylvain Mailler
Supervision: Laurent Menut
Validation: Laurent Menut, Guillaume Siour, Bertrand Bessagnet, Arineh Cholakian, Romain Pennel, Sylvain Mailler
Writing – original draft: Laurent Menut
Writing – review & editing: Laurent Menut, Guillaume Siour, Bertrand Bessagnet, Arineh Cholakian, Romain Pennel, Sylvain Mailler

© 2022 The Authors.
This is an open access article under the terms of the Creative Commons Attribution-NonCommercial License, which permits use, distribution and reproduction in any medium, provided the original work is properly cited and is not used for commercial purposes.

1. Introduction

Mineral dust is an aerosol that plays an important role on air quality and climate evolution. While mineral dust mainly occurs due to natural sources, it has a non negligible impact on air quality and human health (Wang et al., 2020). Mineral dust is mixed with other aerosol and its fine fraction may be counted in the air quality budget and can be ingested by humans (Morman & Plumlee, 2013). At larger spatial scale and over long periods, mineral dust has an important impact on climate evolution with influence on the atmospheric radiative balance, the amount of nutrients in the ocean, the modification of albedo of snow and ice, cloud formation, and precipitation (Carslaw et al., 2010; Schepanski, 2018). The fact that aerosol is added to the troposphere results in changes in radiation and cloud properties; it also has an effect on secondary gas and aerosol species such as ozone. Ozone is particularly sensitive to these changes being produced by photolysis. In addition, the temperature could be modified as well, having also on impact on ozone production (Jenkin & Clemitshaw, 2000; Seinfeld & Pandis, 2006).

Mineral dust emissions are mainly due to three physical mechanisms: saltation, aggregate disintegration and aerodynamic entrainment (Klose et al., 2014). While the first two are dominant when the 10 m wind speed is high (>7 m s^{-1}), the aerodynamic entrainment may become non negligible for low wind speed conditions. In the latter case, it becomes important to well represent the convection effects close to the surface. Parameterizations are developed to take into account this Convective Turbulent Dust Emission, as in Klose and Shao (2012). In addition, wildfires may cause perturbations to the near-surface wind speed; these changes may be due to radiative or convective effects. For example, Lareau and Clements (2015) showed that wildfires may cause density currents, responsible for a modified smoke transport up to 25 km of the wildfire and at speeds up to 4.5 m s^{-1}. The main cause is radiative and due to the difference between the smoke-filled and the smoke-free atmosphere: temperature and boundary layer height are lower under the plume, therefore the mean wind speed is modified. This effect thus

21698996, 2022, 24, Downloaded from https://agupubs.onlinelibrary.wiley.com/doi/10.1029/2022JD037395 by Ecole Polytechnique, Wiley Online Library on [16/12/2022]. See the Terms and Conditions (https://onlinelibrary.wiley.com/terms-and-conditions) on Wiley Online Library for rules of use; OA articles are governed by the applicable Creative Commons License

changes the way the smoke plume is transported and dispersed. The radiative effects of the smoke plume may also have an impact on photochemistry. The shortwave radiation flux can be reduced leading to a decrease in surface ozone concentrations and an increase in daytime NO_2 concentrations (Péré et al., 2015).

In the case of convective events, Cowie et al. (2015) discussed the impact of rare events on the total dust fluxes. The dust emission being a non-linear process depending on the wind speed, rare high wind events may have a large impact on the total emission budget: they showed that, over the region they studied, northern Africa, 25% of the total emissions are due to less than 2% of the events. However, as pointed out by Foroutan and Pleim (2017), convective events are poorly reproduced in meso-scale models, leading to an underestimation of emission flux calculations. They propose to modify the way the calculation is done mainly by (a) changing the mean wind speed by a probability distribution function and take into account gustiness and (b) make data assimilation to improve convective systems modeling. The first change was also made in other studies such as (Menut, 2018) implementing a Weibull distribution to take into account the subgrid scale variability due to the orography variance. Another shortcoming in mineral dust emission modeling is identified as the poor representation of moist convection (haboobs) in regional models. Roberts et al. (2018) estimated that this convection may represent 50% of the emissions in Sahara and Sahel during summer. They show that an explicit representation of convection improves the haboob representation, which then improves the diurnal cycle of wind resulting in better simulation of emitted dust.

Wildfires are also responsible for convective events causing an increase in mineral dust emissions, as presented by Wagner et al. (2018). The study is performed over a limited area of a few hundred square meters and using a large-eddy simulation (LES) model. They discussed the fact that during a fire event, the pyroconvection generates a large thermal wind with important vertical velocities in the updraft. This leads to a wind convergence at the surface with larger wind speed values, which may induce larger mineral dust fluxes if the corresponding surface is erodible. Their study was done at very high resolution (a few meters), for one fire, with a LES (Large Eddy Scale) model. They explore sensitivities of the wind speed changes to several kind of fires, considering grassland and shrubland landuses. The possibility to mobilize more mineral dust is discussed via an academic case at small scale. Dong et al. (2018) also analyzed this phenomenon and linked biomass burning and dust. In the Taklamakan and Gobi deserts, they analyzed several events in which smoke and dust are transported together. But in their case, this is a mixing due to meteorological conditions, and not to a forcing of one by the other. However, they quantified that this mix has an impact on other pollutants such as ozone and nitrogen oxides, leading to severe air pollution episodes. Schlosser et al. (2017) also analyzed aerosol composition after wildfires and showed that mineral dusts are present, explaining that burn front can lift soil dust particles. More recently, Wagner et al. (2021) investigated the impact of agricultural fires on mineral dust emission. They go further on their previous study and investigate the change due to fires on the saltation (via friction velocity) and the convective turbulence (via wind components).

In this study, we consider the interaction between biomass burning and mineral dust emissions. When a fire is detected, the surface is modified to have more favorable conditions for mineral dust emissions. We consider that pyronconvection locally enhances the surface wind speed, and that the soil becomes more erodible, with less vegetation and smaller roughness length. A simple relation is tested to link the two processes. The impact of taking into account this interaction is quantified by simulating gaseous and aerosol species with the WRF-CHIMERE regional modeling system. The additional dust emissions due to fires and their effects on atmospheric concentrations of dust are analyzed, as well as the effects of this additional dust load on radiative fluxes and meteorology. Differences with and without this retroaction are discussed and compared to measurements obtained during the summer 2021 (July and August).

2. The Modeling System

In this section, the whole modeling system is presented, including the WRF and CHIMERE regional models and the way they are coupled online. This also includes how the calculation of the impact of fires pyroconvection on mineral dust was implemented.

21698996, 2022, 24, Downloaded from https://agupubs.onlinelibrary.wiley.com/doi/10.1029/2022JD037395 by Ecole Polytechnique, Wiley Online Library on [16/12/2022]. See the Terms and Conditions (https://onlinelibrary.wiley.com/terms-and-conditions) on Wiley Online Library for rules of use; OA articles are governed by the applicable Creative Commons License

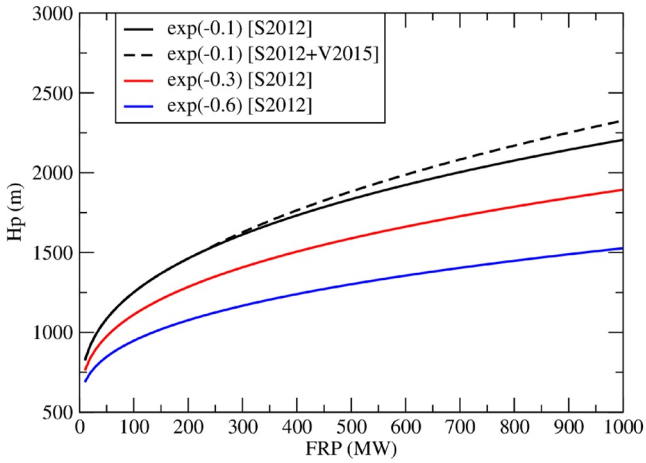


Figure 1. Values of the H_p altitude of the fire plume top as a function of the Brunt-Vaisala number in the free troposphere and as calculated by Sofiev et al. (2012) parameterization. For altitude larger than 1,500 m, Veira et al. (2015) is applied.

2.1. The WRF and CHIMERE Models

The regional models WRF 3.7.1 (Powers et al., 2017), and CHIMERE 2020r3 (Menut et al., 2021), are used. This version of CHIMERE is designed to take into account (in online mode) or not (in offline mode) the direct and indirect effects of aerosols on radiation and cloud properties. The way these effects are taken into account is described in Briant et al. (2017) (for the direct effects) and Tuccella et al. (2019) (for the indirect effects). The model configuration is exactly the same as in Menut et al. (2021): it includes emissions from anthropogenic, biogenic, sea-salt, biomass burning, lightning NO_x and mineral dust sources. It also includes gaseous and particulate chemistry for tens of species and with 10 size distribution bins for aerosols. In this study, the WRF-CHIMERE system is used in online mode. The spectral nudging above the Planetary Boundary Layer is activated to avoid possible divergence of the model so that it is constrained by the meteorological forcing taking observations into account. The model domain is defined with the same horizontal grid for WRF and CHIMERE and covers the whole Europe and a part of Asia: 170×90 cells with a constant resolution of 50 km. The WRF model has 32 vertical levels from the surface to 50 hPa. CHIMERE has less vertical levels, 20 layers from the surface to 200 hPa (and variables are interpolated during the coupling when exchanges are made between the two models).

2.2. The Biomass Burning Emission

The biomass burning emission fluxes are diagnosed from the CAMS data set (Kaiser et al., 2012). These fluxes are proposed as surface fluxes with a $0.1 \times 0.1°$ horizontal resolution. Then, they are remapped on the CHIMERE horizontal grid, aggregated into the model species and vertically redistributed. The fluxes are also converted from daily to hourly bases using a diurnal profile.

Vertically, the surface flux redistribution is a key point. First the injection height, H_p, is diagnosed following the schemes of Sofiev et al. (2012) and Veira et al. (2015). The calculation used the Convective Available Potential Energy estimation being diagnosed using the Fire Radiative Power (FRP) for each fire, as:

$$H_p = \alpha H_{abl} + \beta \left(\frac{P_f}{P_{f0}} \right)^{\gamma} \exp\left(-\frac{\delta N_{FT}^2}{N_0^2} \right) \quad (1)$$

with $\alpha = 0.24$, $\beta = 170$ m, $\gamma = 0.35$, $\delta = 0.6$, $P_{f0} = 10^6$ W and $N_0^2 = 2.4 \times 10^{-4}$ s^{-2}. The FRP, P_f, is in Watts. N_{FT} is the Brunt-Väisälä frequency in the free troposphere. An empirical correction is performed for the known underestimation of FRP by MODIS in case of strong fires (Veira et al., 2015):

$$P_f^* = P_f \times \left(\frac{H_p}{H_{deep}} \right)^{\epsilon} \quad (2)$$

with $\epsilon = 0.5$ and $H_{deep} = 1{,}500$ m. An example of H_p calculation is presented in Figure 1 as an academic case, by applying only the equation for fixed values of the ratio of $\delta N_{FT}^2 / N_0^2$. The curves include examples with ratios equal to -0.1, -0.3 and -0.6 with the Sofiev et al. (2012). For the example with the ratio equal to -0.1, we also present the mix between Sofiev et al. (2012) (for $H_p \leq 1{,}500$ m) and Veira et al. (2015) (for $H_p > 1{,}500$ m). It shows that for FRP between 0 and 1,000 MW, H_p varies between 700 and 2,500 m. In the model, the FRP values are provided hourly by the CAMS fire data set and the Brunt-Väisälä frequency is calculated at each physical time-step (a few minutes depending on the meteorology). There are some differences in the treatment of the FRP compared to the previous CHIMERE model version, described in Menut et al. (2021). In this study, we use the FRP product proposed by CAMS directly, (Rémy et al., 2017). A diurnal profile is applied, as the one used for the chemical species (as in Menut et al. [2021], but with the minimum and maximum values used in Gonzi et al. [2015], between 0.2 and 1).

21698996, 2022, 24, Downloaded from https://agupubs.onlinelibrary.wiley.com/doi/10.1029/2022JD037395 by Ecole Polytechnique, Wiley Online Library on [16/12/2022]. See the Terms and Conditions (https://onlinelibrary.wiley.com/terms-and-conditions) on Wiley Online Library for rules of use; OA articles are governed by the applicable Creative Commons License

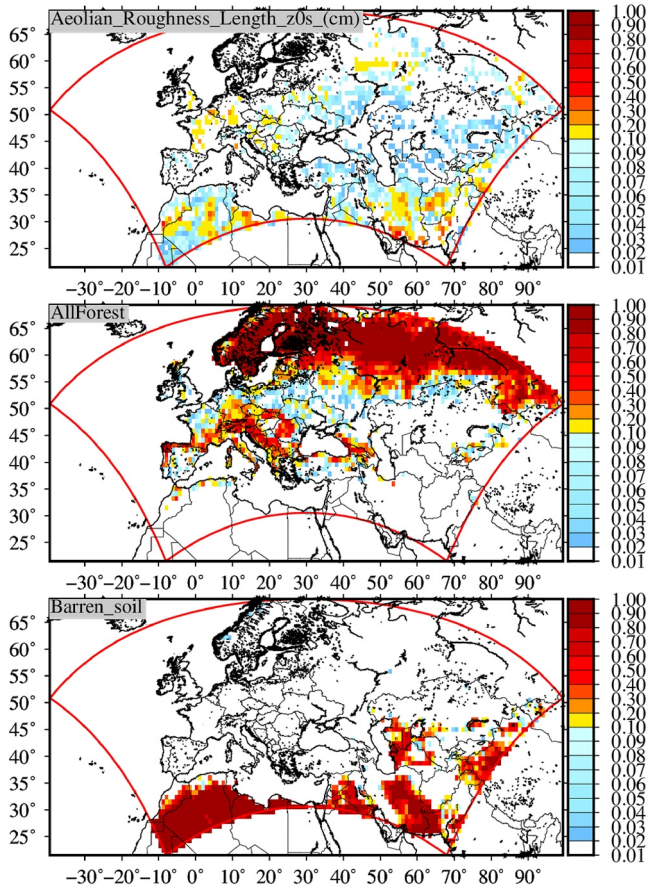


Figure 2. The simulation domain and some surface characteristics. The map with z_0 (cm) corresponds to the saltation roughness length, "Forest" to the area fraction occupied by forests [0:1], "Barren," the area fraction occupied by barren soil [0:1].

Second, the shape of the vertical profile uses K_z-like shape that is, a local maximum with a slow decrease with altitude. Here we use two maxima: one in the surface layer and one around H_p. These configurations are described and used in Menut et al. (2018) (see Figure 2) and Menut et al. (2021). There is no subgrid scale variability in the calculation of these fluxes: fluxes are considered as averaged over the grid cell surface, even if the fire was small compared to this surface. Although the estimation of biomass burning emissions remains very uncertain (Ye et al., 2021), it is not an important limitation for this study: the most important point is not the accuracy of the absolute value of the flux, but its correct localization in time and space, since we want to estimate the impact of fires outbreaks on mineral dust emissions.

2.3. The Mineral Dust Emission

The mineral dust emissions are calculated using the Alfaro and Gomes (2001) scheme, optimized following Menut et al. (2005). The emission depends on many parameters, including the surface properties of each model grid cell. These properties are presented in Figure 2: z_0 corresponding to the saltation roughness length (the first marker of erodible surfaces). The "Forest" and "Barren" landuse categories represent the fraction area for these environments as example of all landuse considered in the model. Mineral dust could be emitted over barren surfaces, shrubland, cropland, grassland but not over forest or wetland (Menut et al., 2013). A good indicator of erodible surfaces is to consider the locations where we have at the same time a low roughness length value and a landuse corresponding to an erodible surface. The emission also strongly depends on the mean wind speed in the grid cell, defined as:

$$U = \sqrt{U_r^2 + (1.2 w_*)^2} \tag{3}$$

with U the mean wind speed used for the emission flux calculation, U_r the grid resolved wind speed simulated by the meteorological model, and w_* the convective velocity scale to take into account the convective effects.

In order to take into account the sub-grid scale variability, flux calculations are done following several steps. First, sub-fluxes are calculated for each soil type of the grid cell. Second, for each soil type, the flux is also calculated for each landuse. For each sub-flux, the same meteorological variables are used: precipitation, soil humidity and wind speed because they represent the mean value in the grid cell. To take the possible subgrid scale wind variability into account, a Weibull distribution is applied as described in Menut et al. (2005). Depending on the orography variance in the grid cell, the k shape parameter of the Weibull distribution is modified (Menut, 2018). For each grid cell, the final mineral dust flux is thus the addition of several sub-grid fluxes as:

$$F = \sum_{i=1}^{N_{soil}} \sum_{j=1}^{N_{landuse}} \sum_{k=1}^{N_{wind}} F(i,j,k) \tag{4}$$

After emission, the mineral dust is transported and deposited. The mineral dust aerosol has properties such as its density $\rho_p = 2.65$ g.cm^{-3}, and its optical properties for the five wavelengths used with the FastJX photolysis model (Wild et al., 2000). The refractive index is defined with its real (R) and imaginary (I) parts. For the real part, $R = 1.53$ for all wavelengths. For the imaginary part, $I = 5.5e^{-3}$ at $\lambda = 200$ nm, $I = 5.510^{-3}$ at $\lambda = 300$ nm, $I = 2.410^{-3}$ at $\lambda = 400$ nm, $I = 8.910^{-4}$ at $\lambda = 600$ nm, and $I = 7.610^{-4}$ at $\lambda = 999$ nm. These values are taken from the ADIENT project, (as described in Mailler et al. [2016]) and were used for validation in Briant et al. (2017) and Tuccella et al. (2019).

21698996, 2022, 24, Downloaded from https://agupubs.onlinelibrary.wiley.com/doi/10.1029/2022JD037395 by Ecole Polytechnique, Wiley Online Library on [16/12/2022]. See the Terms and Conditions (https://onlinelibrary.wiley.com/terms-and-conditions) on Wiley Online Library for rules of use; OA articles are governed by the applicable Creative Commons License

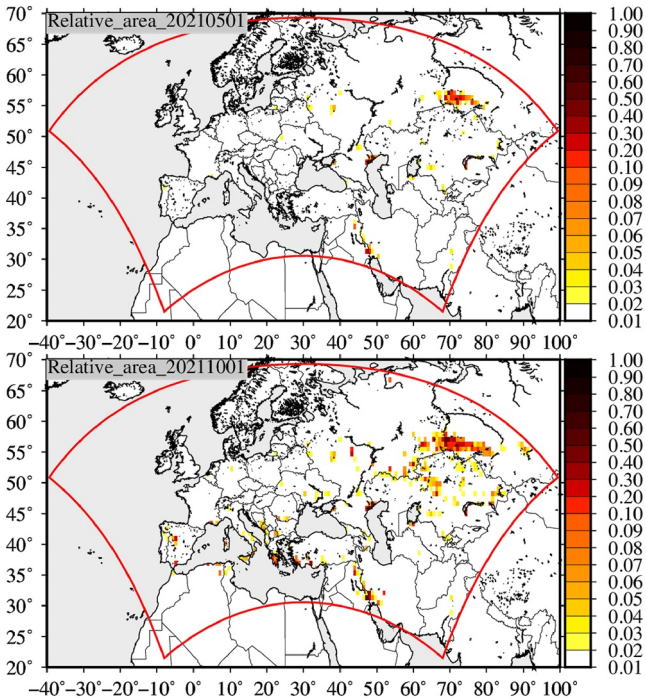


Figure 3. Estimation of accumulated burnt area fraction over the modeled domain. Examples are presented for 1 May 2021 and 1 October 2021.

2.4. Model Developments

The model developments are dedicated to link the mineral dust emission to the biomass burning events. The starting version is the distributed v2020r3 CHIMERE version and only the fires and mineral dust emission schemes are changed for this study. Biomass burning fluxes have to be first diagnosed, including the fire radiative power, the burnt area and the injection height. Depending on these parameters, it is possible to parameterize an additional surface wind speed value and modify the soil and surface characteristics for the mineral dust emissions. These changes will only apply for mineral dust emission, but not for the other processes.

For the following developments, a lot of uncertainties exist and must be discussed. In this model version, several hypotheses were made, each time in the more realistic way. The main goal of this study is to evaluate if, at the regional scale, biomass burning has a significant impact on mineral dust emission. Our various hypotheses in this study make it possible for us to answer this question. However, regarding the exact magnitude of this impact, uncertainties still remain.

Two main changes are done in the model to take into account the impact of fires on dust emissions:

- The change of soil and surface characteristics in the grid cell where a fire is diagnosed.
- The change of 10 m wind speed used for mineral dust emission

2.4.1. Change in Soil and Surface Characteristics

The soil and surface change is an important point for this study, because a fire may induce a more erodible nature. This change is also relatively unknown at the regional scale and several hypothesis have to be made.

The first hypothesis regards the surface of the burnt area. This information is not provided with the data used. Some products exist with other biomass burning models, but these data are still uncertain. In addition, the CAMS data are recognized to have accurate results on the location and intensity of fire fluxes and there is a strong interest to use it in the framework of the WRF-CHIMERE system when used in the Copernicus CAMS daily forecast. For this study, the hypothesis is made that the burnt surface should be proportional to the fire radiative power via the fire size. It is not strictly exact but corresponds to a correct first guess as quantified by Yue et al. (2014) and (Laurent et al., 2019). This enables us to calculate a relative fraction of the CAMS grid cell (with resolution $0.1 \times 0.1°$). For each day of fire data, the new burnt surfaces are added to the previous days in a cumulative fashion. The accumulation starts the 1 January 2021. Examples of maps during the year 2021 are presented in Figure 3.

The second hypothesis is about the change of soil and surface properties. The goal is to just consider that the burnt surface is more erodible. Without impact of fires on dust, the erodibility is diagnosed for each grid cell, and each percentage of landuse and soil in this specific cell. The MODIS product adapted by Beegum et al. (2016) is used. This satellite product being mostly accurate over the desert, the landuse is screened for the model cell using the USGS data used for the simulation. In case of erodible but non-desert cells, the erodibility is estimated as the surface (1.-greenfrac), "greenfrac" being the USGS vegetation fraction used by the meteorological part of the modeling system, WRF. In case of fires, soil and surface properties are thus changed for the area fraction of the model grid cell, considering that: (a) the soil moisture becomes 0.1 $kg \cdot kg^{-1}$ to represent a dry soil, (b) the aeolian roughness length becomes $z_0 = 0.01$ cm to represent an erodible surface, (c) the soil becomes sand to have properties of erodible material and to be closer to soil after burning such as what is presented by the Chernozemic soils studied with the same model in Bessagnet et al. (2008), and (d) the erodibility (measured by MODIS) is considered as 100% for the burnt fraction area.

21698996, 2022, 24, Downloaded from https://agupubs.onlinelibrary.wiley.com/doi/10.1029/2022JD037395 by Ecole Polytechnique, Wiley Online Library on [16/12/2022]. See the Terms and Conditions (https://onlinelibrary.wiley.com/terms-and-conditions) on Wiley Online Library for rules of use; OA articles are governed by the applicable Creative Commons License

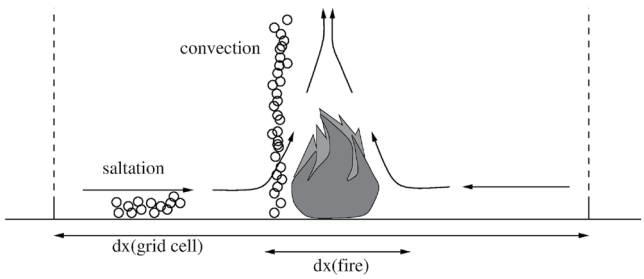


Figure 4. Principle of the impact of wildfires on wind speed in a model grid cell: the fire induces more surface wind speed and then more saltation, and more convection.

2.4.2. Change on 10 m Wind Speed

As displayed in Figure 4, the fire may change the mean wind speed in two ways: (a) an increase at the surface and (b) an increase of vertical transport due to pyroconvection.

For the increase of wind speed at the surface, we propose a simple relationship between the FRP and the mean wind speed. For the sake of realism, we can only compare our equation to the calculations at high spatial resolution data presented in Wagner et al. (2021). This study is a keystone for the topic of wildfire-driven mineral dust emissions: LES modeling is used and an order of magnitude of the impact is clearly estimated and presented. We thus can consider this study as a reference for this geophysical problem. An extra term of wind speed due to a fire in the grid cell may be expressed as:

$$\Delta U_{10m} = \frac{u_c}{1 + u_a \exp(-u_b \times FRP)} \quad (5)$$

with the FRP between 0 and 1,000 MW. Equation 5 implements a logistic sigmoid function, with maximal value $u_c = 3$ m s^{-1}, $u_a = 100$, growth rate $u_b = 0.01$ MW^{-1}. This equation ensures a smooth relationship between ΔU and FRP, with $\Delta U = \frac{u_c}{2}$ for $FRP = 460$ MW. The value of u_c is arbitrary and was selected to be realistic. Figure 5 presents Equation 5 with the additional 10 m wind speed, $\Delta U_{10\,m}$, as a function of the FRP (MW) in a grid cell. For example, three values of the parameter u_c are used with $u_c = 2$, 3, and 5 m.s^{-1}.

Unfortunately, there is no data that can be used as constraint to fit these parameters. The only way to qualify these values is to perform regional simulations and to quantify the impact on available observations. For the convective effects due to the pyroconvection, we add a direct injection term of the emitted dust in the boundary layer, up to the H_p calculated for the wildfire emissions.

The two effects are summarized in Figure 6: in the first case, *DFno*, the surface wind speed is represented by a Weibull distribution. Only wind values above the wind threshold U_t are used to calculate mineral dust emissions. Dust emissions are injected in the first model vertical grid cell only. In case of a link between fires and dust, the fluxes are expressed as *DFvert*. The surface wind speed is larger, then more wind values are up to U_t: the mineral dust emission flux is larger. In addition, considering that pyroconvective effect transports surface emissions in the boundary layer, a wildfire-driven vertical profile of dust emissions is applied. This profile represents a uniform distribution of the dust in all levels from the surface to H_p.

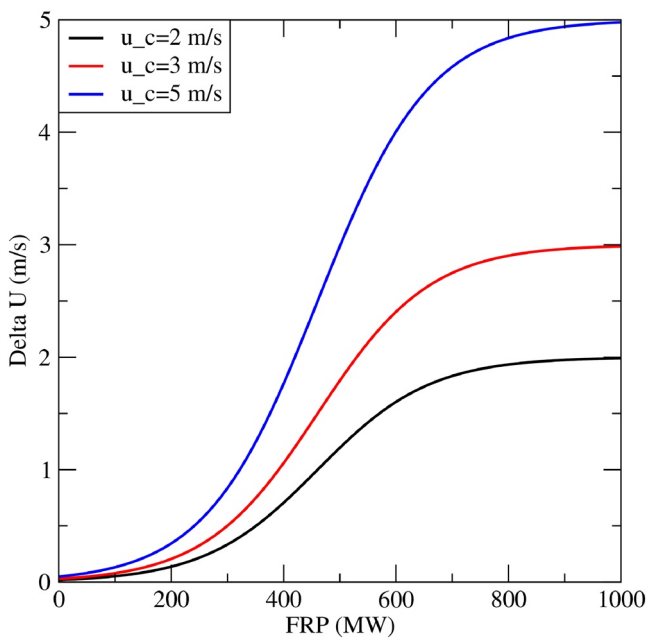


Figure 5. Equation 5 linking the additional 10 m wind speed, ΔU_{10m} to the FRP (MW). Three values of the parameter u_c are used with $u_c = 2$, 3, and 5 m·s^{-1}.

2.5. The Test Case and the Observation Data

The test case corresponds to the summer of 2021, from 1 July to 31 August and for the whole Europe and a part of Asia. During this period, numerous fires were observed as described by the European Forest Fire Information System (EFFIS) web site with daily biomass burning maps (https://effis.jrc.ec.europa.eu). Two main spots are observed: in Russia, as already studied by Konovalov et al. (2011), Konovalov et al. (2015), and in Greece as already studied by Hodnebrog et al. (2012), Rea et al. (2015), and among many others. The simulation domain is presented in Figure 7. This Figure also presents the sum of wildfire flux of Carbon Monoxide (CO) during the months of July and August 2021.

Two simulations will be compared in this study, corresponding to notations in Figure 6:

- "DFno": A simulation with all possible emissions including fire and mineral dust. It corresponds to the usual configuration of the WRF-CHIMERE model used for analysis or for forecast.

21698996, 2022, 24, Downloaded from https://agupubs.onlinelibrary.wiley.com/doi/10.1029/2022JD037395 by Ecole Polytechnique, Wiley Online Library on [16/12/2022]. See the Terms and Conditions (https://onlinelibrary.wiley.com/terms-and-conditions) on Wiley Online Library for rules of use; OA articles are governed by the applicable Creative Commons License

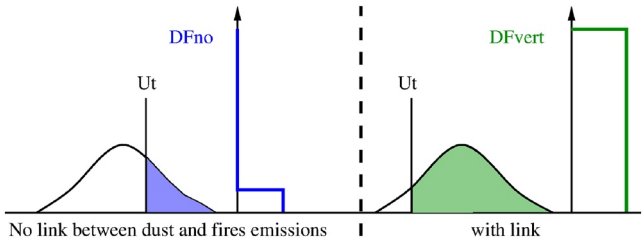


Figure 6. Schematic plot of the principle of the impact of wildfires on mineral dust emissions. On the left side, when there is no link between dust and fire emissions, the emissions DFno are moderate and only injected in the first vertical level. When the link is taken into account, the flux DFvert is with more emissions at the surface and is injected upto the altitude of the fires injection height.

- "DFvert": Same configuration as "DFno" but with the impact of fires on mineral dust emissions.

For the impact at the surface, the simulation results will be compared to particulate matter, $PM_{2.5}$ and PM_{10} surface concentrations. Mineral dust having also an impact on radiative transfer, then photochemistry, comparisons are also performed with surface ozone concentrations. All measurements are hourly and come from the European Environment Agency (EEA, https://www.eea.europa.eu) database. Stations are presented in Figure 8. For the impact on the whole troposphere, we compare the simulation results to aerosol optical depth (AOD) data taken from the AErosol RObotic NETwork global remote sensing network (AERONET, https://aeronet.gsfc.nasa.gov), (Holben et al., 2001) and the inversion product providing aerosol size distribution (Dubovik & King, 2000).

For the vertical structure of the troposphere with aerosol, the CALIOP lidar is used. It is on-board the Cloud-Aerosol Lidar Pathfinder Satellite Observation (CALIPSO) satellite (Winker et al., 2010). The product is used to obtain an aerosol sub-type classification (CALIOP v4.10 product). Aerosol classification was developed by Omar et al. (2010) and Burton et al. (2015). It provides information on the vertical extent of aerosol layers. The aerosol sub-type classification is built on thresholds of lidar-derived optical characteristics and remains uncertain, its limitations are described in Tesche et al. (2013). With CHIMERE, a specific development was implemented for the comparison between CALIOP and the model results. It is described in detail in Menut et al. (2018).

The different periods presented in this study are:

- From 1 January to 31 December 2021: analysis of the fire emissions and storage of the burnt locations and landuse and soil changes.
- From 1 July to 31 August 2021: simulation with WRF and CHIMERE over Europe.
- From 15 to 31 August 2021: refinement of the analysis of the impact on fires on dust emissions.

3. Impact on Mineral Dust Emissions and Meteorology

3.1. Impact on Emissions

The first quantified impact is on mineral dust emissions. Results are presented in Figure 9. First, a map of emissions averaged over the last two weeks of the simulated period, from 15 to 31 August 2021 is presented. Emissions are with the "DFno" test case, meaning that the model has no changes compared to the reference CHIMERE version v2020r3. It shows that emissions are mainly located in two areas: Algeria and East of the domain (Kazakhstan, Uzbekistan, Turkmenistan). The second map shows the differences of time-averaged emissions between "DFvert" and "DFno." The first area, around Algeria, does not show differences, highlighting no impact of fires on dust emissions. In this case, it is because the area is mainly desert and fires did not occur in this region. Very low negative values are observed, showing the impact on mean wind speed, discussed later in Section 4.3. It is not the case for the second region where differences are important: the region was originally erodible, but also contains vegetation susceptible of burning which results in an increase of the already present erodible surfaces. It shows that the most important impact of the changes made in the model will be in this area. Unfortunately, it is not a region where a lot of observations are available. A third region of dust emissions is visible, at the North of the second one and corresponding to the area where fires were observed during August 2021, at the border between Kazakhstan and Russia. This area is a prominent example the effect of fires on mineral dust emission.

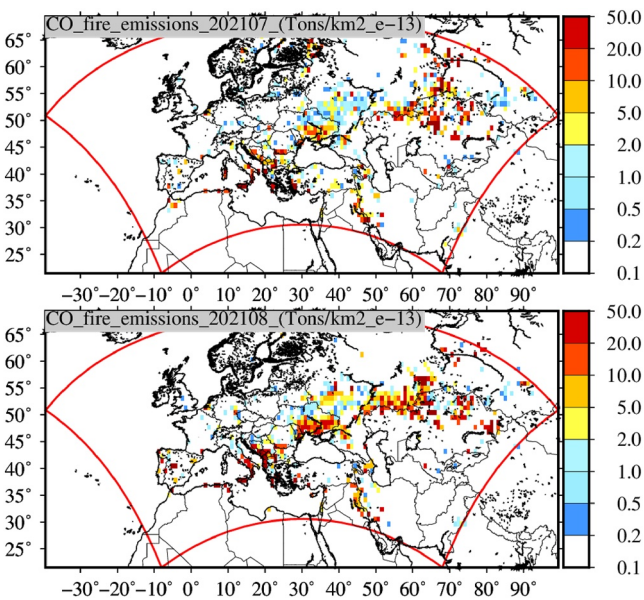


Figure 7. Cumulative fire fluxes during the months of July and August 2021 for carbon monoxyde, CO (molecules $cm^{-2}\ s^{-1} \times 10^{-15}$).

21698996, 2022, 24, Downloaded from https://agupubs.onlinelibrary.wiley.com/doi/10.1029/2022JD037395 by Ecole Polytechnique, Wiley Online Library on [16/12/2022]. See the Terms and Conditions (https://onlinelibrary.wiley.com/terms-and-conditions) on Wiley Online Library for rules of use; OA articles are governed by the applicable Creative Commons License

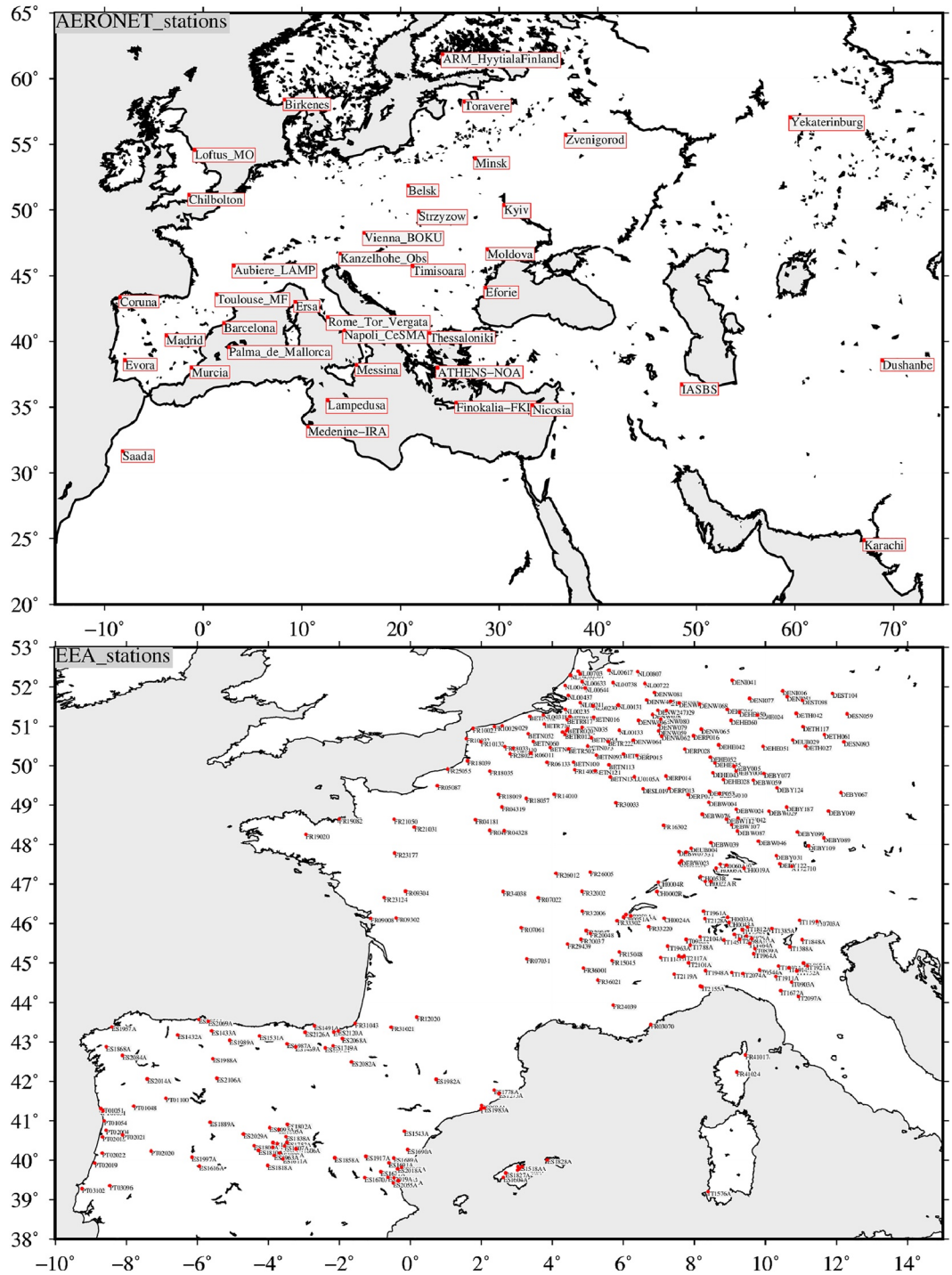


Figure 8. Maps of AERONET and EEA stations used.

3.2. Variability of Meteorology

Very few meteorological data are available in the Eastern part of the domain, where wildfires are observed and mineral dust may be additionally emitted. 2m temperature and 10m wind speed are available at the station of Petropavlovsk (UACP, Kazakhstan) (latitude 54.78°N and longitude 69.18°E). Comparison between the measurements and the two simulations is displayed in Figure 10.

21698996, 2022, 24, Downloaded from https://agupubs.onlinelibrary.wiley.com/doi/10.1029/2022JD037395 by Ecole Polytechnique, Wiley Online Library on [16/12/2022]. See the Terms and Conditions (https://onlinelibrary.wiley.com/terms-and-conditions) on Wiley Online Library for rules of use; OA articles are governed by the applicable Creative Commons License

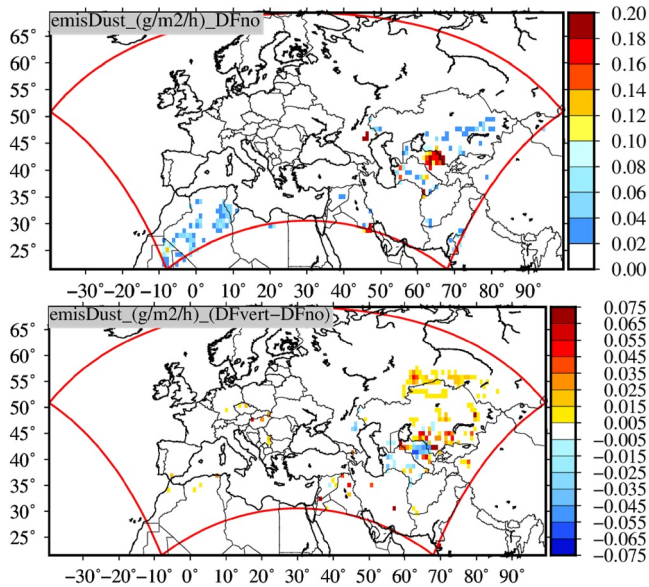


Figure 9. Maps of time-averaged (from 15 to 31 August 2021) mineral dust emissions for "DFno" and differences between simulations calculated as "DFvert" minus "DFno."

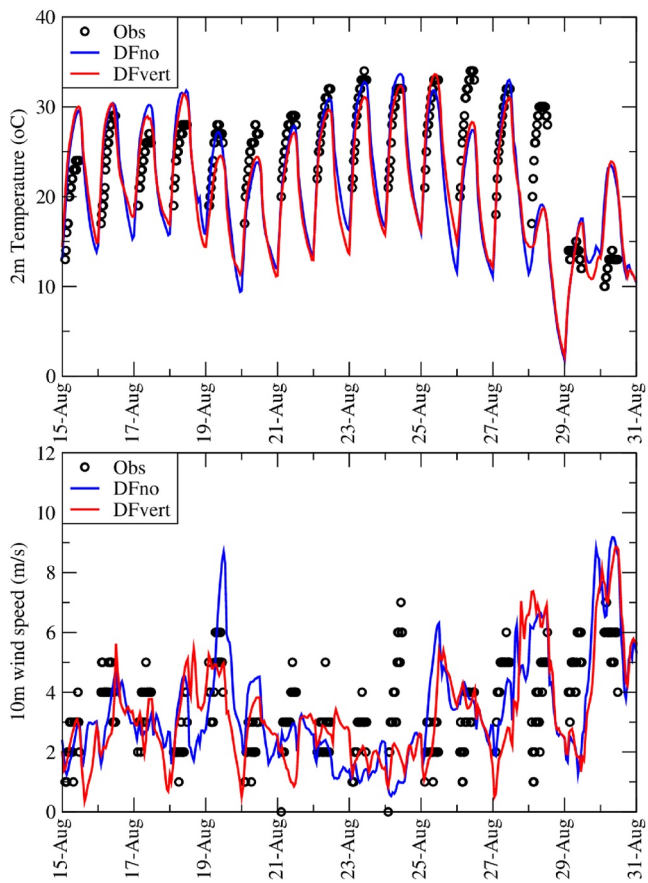


Figure 10. Two meter temperature and 10 m wind speed measured at station Petropavlovsk (UACP, Kazakhstan) and modeled with WRF-CHIMERE and for simulations DFno and DFvert. The period is from 15 to 31 August 2021.

Comparison shows that the model is able to reproduce the 2 m temperature. From observations, the mean temperature increase during the month of July and beginning of August, until a sudden decrease from 27 August to 31 August. The model reproduces this decrease for the end of the period, but with a variability that is too large. For the minimum temperatures, the model underestimates the observed values during the night, probably a problem of representativity and subgrid scale orography variability when we compare a local measurement to a mean averaged model grid cell. But during the day, the maximum values are well reproduced. It is the same conclusion for 10m wind speed: the two simulations are different but the observation data (recorded with a poor accuracy of 1 $m \cdot s^{-1}$) varies between 1 and 10 $m\ s^{-1}$ and are not closer than one simulation or the other.

4. Impact on Atmospheric Concentrations and AOD

In this section, we compare modeled results to available data recorded at the surface (in situ or vertically integrated). First, AOD and Angström exponent (ANG) time-series are compared to AERONET data. Second, maps of surface concentrations of pollutants are presented. For aerosols, mineral dust concentrations illustrate the impact of the change proposed in this study. For gaseous species, surface ozone concentrations are presented, being a secondary species highly sensitive to variations in radiation and temperature. It is also a long-lived species (several days), then it is interesting to see if changes are impacting remote areas. For the same species, vertical cross-sections are also presented. Third, aerosol size distributions are presented for some sites where the inverted AERONET data are available.

4.1. Time-Series of Aerosol Optical Depth and Angström Exponent

Time series are presented in Figure 11 for AOD and ANG. Data are from the AERONET database v.1.5 (Figure 8) and are averaged daily same as the model results. Athens (Greece), IASBS (Iran) and Dushanbe (Tajikistan) stations are selected because an effect is visible and they correspond to the available data closest to the fire areas. For many other stations, no change (or negligible changes) were observed. For all locations, AOD is under-estimated by the model, independently of the configuration DFno or DFvert. Despite this bias, the time variability is realistic for a major part of the stations, except Dushanbe. The differences between DFno and DFvert are low in Athens but non negligible in IASBS and Dushanbe. For ANG, the comparison shows that the variability of the aerosol size distribution is well reproduced by the model. In Athens there is mainly fine particles, when they are coarser in IASBS and clearly coarse in Dushanbe. ANG remains close between DFno and DFvert in Athens, mainly because the impact of the additional emissions is not important. In IASBS, ANG is less correct with DFvert: adding mineral dust induces having too coarse aerosol size distribution. In Dushanbe, the opposite happens: ANG is modeled better with DFvert. The Angstrom exponent variability is due to transport of mineral dust over this region, because in all cases, modeled aerosol are more coarse. The fact to have worst scores in IASBS is due to the fact that in the DFno configuration the model is already biased: Angstrom exponent is well modeled but it is certainly a compensation of errors. For this specific case, the biased emission then transport of mineral dust may be due to several factors: (a) the soil characteristics and its humidity is less well represented in the databases or by the meteorological model, (b) the 10 m wind speed used as dust is less well diagnosed over IASBS than

21698996, 2022, 24, Downloaded from https://agupubs.onlinelibrary.wiley.com/doi/10.1029/2022JD037395 by Ecole Polytechnique, Wiley Online Library on [16/12/2022]. See the Terms and Conditions (https://onlinelibrary.wiley.com/terms-and-conditions) on Wiley Online Library for rules of use; OA articles are governed by the applicable Creative Commons License

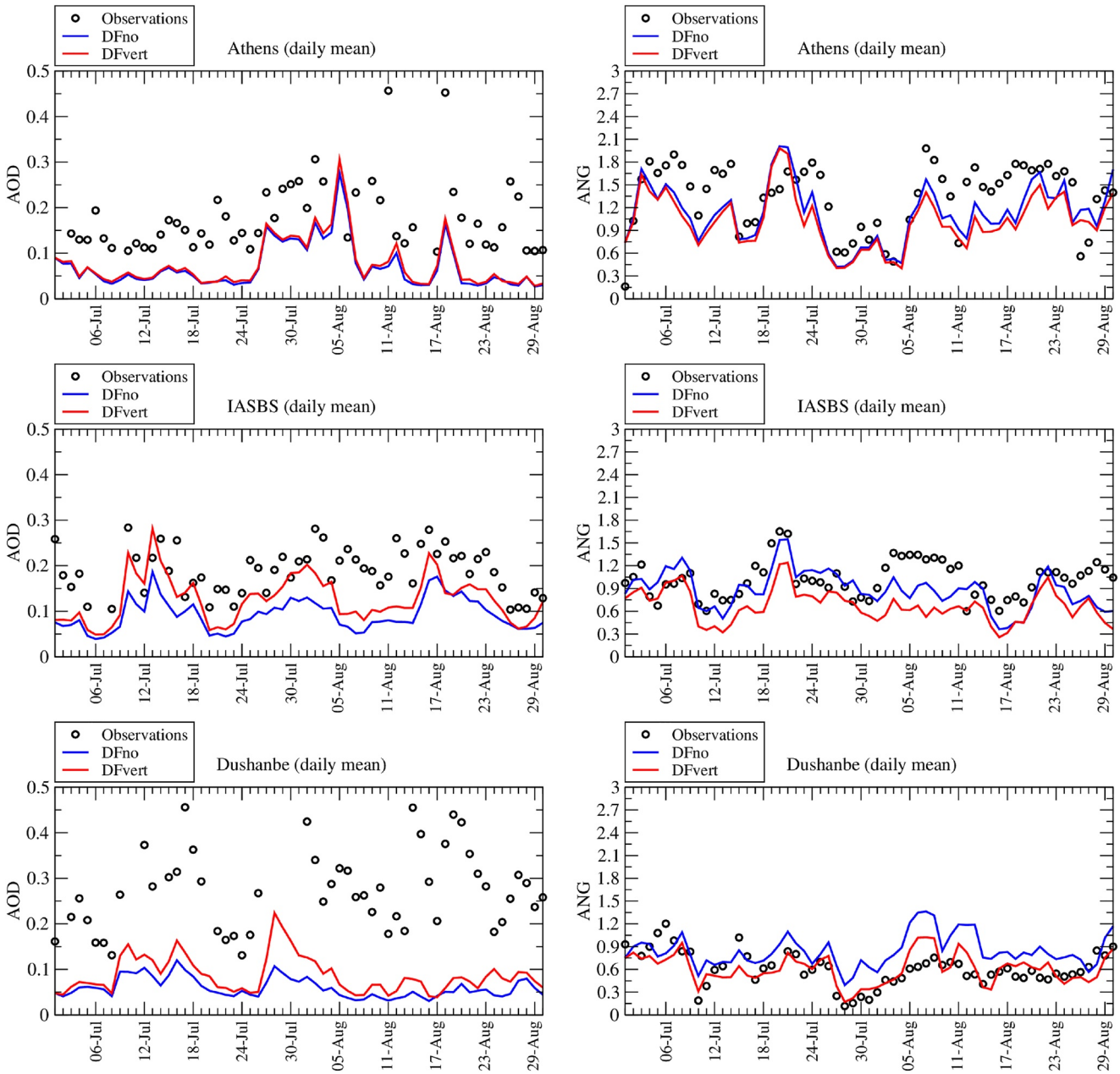


Figure 11. Time-series of Aerosol Optical Depth and Angström exponent. The comparison is performed between observation data from AERONET and modeled data for the WRF-CHIMERE simulations. Results are presented for the AERONET stations of Athens, IASBS, and Dushanbe.

over other sites such as Athens of Dushanbe, (c) the boundary layer characteristics are less well estimated leading to more transport of deposition. Due to the lack of observations in this region, it is difficult to identify and quantify the reason.

Time-series comparisons were also performed for surface ozone and particulate matter, $PM_{2.5}$ and PM_{10}. But, for these variables, the differences between model configurations DFno and DFvert were so low that we determined there is no interest in presenting them. However, it is important to note that no specific bias was calculated for PM. Therefore, the bias of AOD is not due to a problem of mass underestimation over the whole size distribution.

21698996, 2022, 24, Downloaded from https://agupubs.onlinelibrary.wiley.com/doi/10.1029/2022JD037395 by Ecole Polytechnique, Wiley Online Library on [16/12/2022]. See the Terms and Conditions (https://onlinelibrary.wiley.com/terms-and-conditions) on Wiley Online Library for rules of use; OA articles are governed by the applicable Creative Commons License

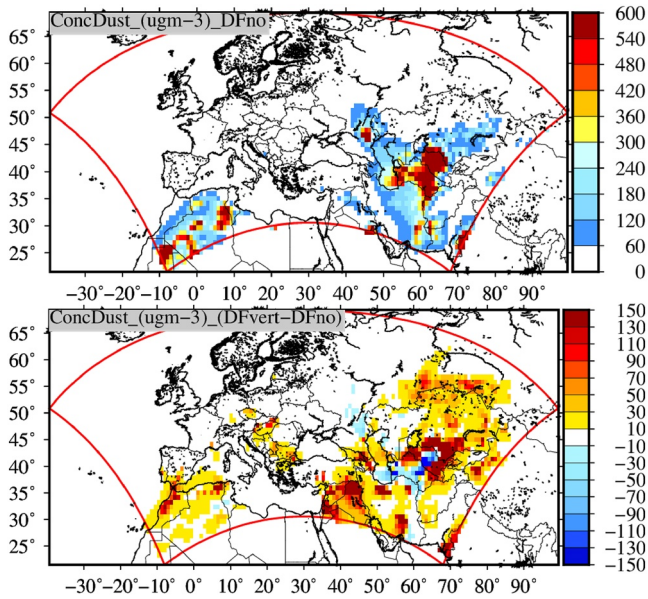


Figure 12. Surface concentration maps of mineral dust (in $\mu g \cdot m^{-3}$). Values are for the DFno simulation and the differences between DFno and DFvert. Values are averaged over the period 15–31 August 2021.

4.2. Concentrations of Mineral Dust

Results are presented as time-averaged maps and the average interval is limited to the period from 15 to 31 August 2021. This choice is made to have more realistic averaged maps than if we had averaged over the entire 2-month period. Figure 12 presents surface concentrations of mineral dust (in $\mu g\ m^{-3}$). The map is presented for the concentrations for the DFno simulation and in term of differences (DFvert-DFno). For DFno, two main areas of high concentrations are displayed, corresponding to the most emitting areas as presented in Figure 9. They correspond to the South-Eastern (Morocco) and South-Western (Kazakhstan, Uzbekistan) parts of the modeled domain. It corresponds mainly to barren surfaces where some fires were also observed. The map of differences shows new areas with mineral dust concentrations: they correspond to the new process linking wildfires and dust emissions. At the latitude 50°N, many new emitted areas are present in Russia (around Omsk, Novossibirsk). Around latitude +35°N, from Saudi Arabia to Syria, different regions appear with additional emissions.

Vertical cross-section is displayed in Figure 13. Values are presented for an iso-latitude transect, values being averaged for latitudes between 35° and 45°N. Values are also time-averaged for the simulated period, from 15 to 31 August 2021. Values are then displayed in longitude and altitude, as differences between the two simulations. The increase appears at the East of the domain and is significant until an altitude of 3,000 m AGL. The most important differences remain in the boundary layer (the gray line in the Figure).

Figure 14 presents a comparison between the CALIOP aerosol product and the same analysis with the CHIMERE simulations. The CALIOP classification is for the transects of 16 (08:40 UTC) and 26 (22:23 UTC) August 2021 over Europe. The data are displayed along the latitude, from ≈20° to 65°N. The original trajectory is displayed in Figure 15. Several structures are present: mainly mineral dust in the southern part but mainly pollution dust in the northern part. For the 16 August, the CALIOP detection algorithm diagnoses a mix of several aerosols all along the transect, including dust, pollution smoke and pollution dust. With the simulation DFno, there is no aerosol attribution above latitude 48°N even if there are present in the measurements. These aerosols are present in the DFVert simulation with "polluted dust." This comparison shows that the mineral dust emissions increase the realism compared to the CALIOP data. For the 26 August and in altitude, between 6 and 8 km, a mix of several aerosols is observed with clean layers, elevated smoke and polluted dust. But these may be of other origin, the uncertainty remaining important with this type of interpreted data. With the two simulations, DFno and DFvert, the main vertical structure is well modeled. Some differences appear between the two model configurations. Mainly, the aerosols are not the same around the latitude 50°N when the classification changes to "polluted smoke" for DFvert where it was "Not Attributed" for DFno. The shape of the structures are slightly different between the two simulations as well, mainly showing that the additional mineral dust emissions change the atmospheric composition until an altitude of 6,000 m for this transect.

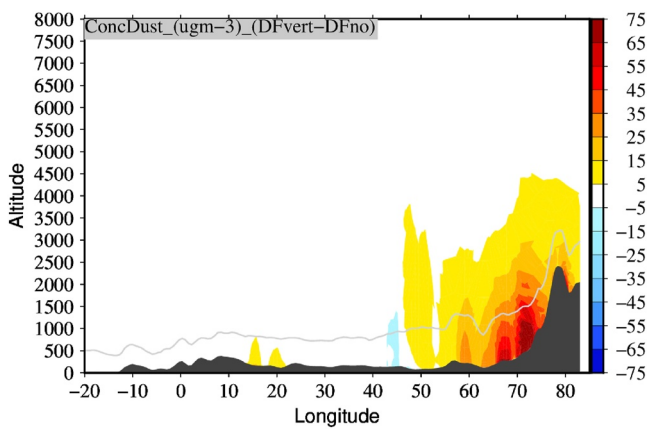


Figure 13. Vertical cross-sections of mineral dust concentrations as differences DFvert minus DFno. Values are time-averaged for latitudes between 35° and 45°W and for the period 15–31 August 2021. The gray line indicates the mean averaged value of the boundary layer.

4.3. Impact on Other Variables

The fact that adding mineral dust concentration changes the atmospheric composition means that it will then modify the meteorological variables and other pollutants concentrations as a consequence. This realistic effect is modeled with the online version of the WRF-CHIMERE modeling system.

The map of surface ozone concentrations, Figure 16, shows that values range from 10 to 80 ppb in average during the period. Concentrations are increasing with decreasing latitude, due to the increasing radiation and air temperature. The map of differences (DFvert-DFno) has no specific pattern. The most

21698996, 2022, 24, Downloaded from https://agupubs.onlinelibrary.wiley.com/doi/10.1029/2022JD037395 by Ecole Polytechnique, Wiley Online Library on [16/12/2022]. See the Terms and Conditions (https://onlinelibrary.wiley.com/terms-and-conditions) on Wiley Online Library for rules of use; OA articles are governed by the applicable Creative Commons License

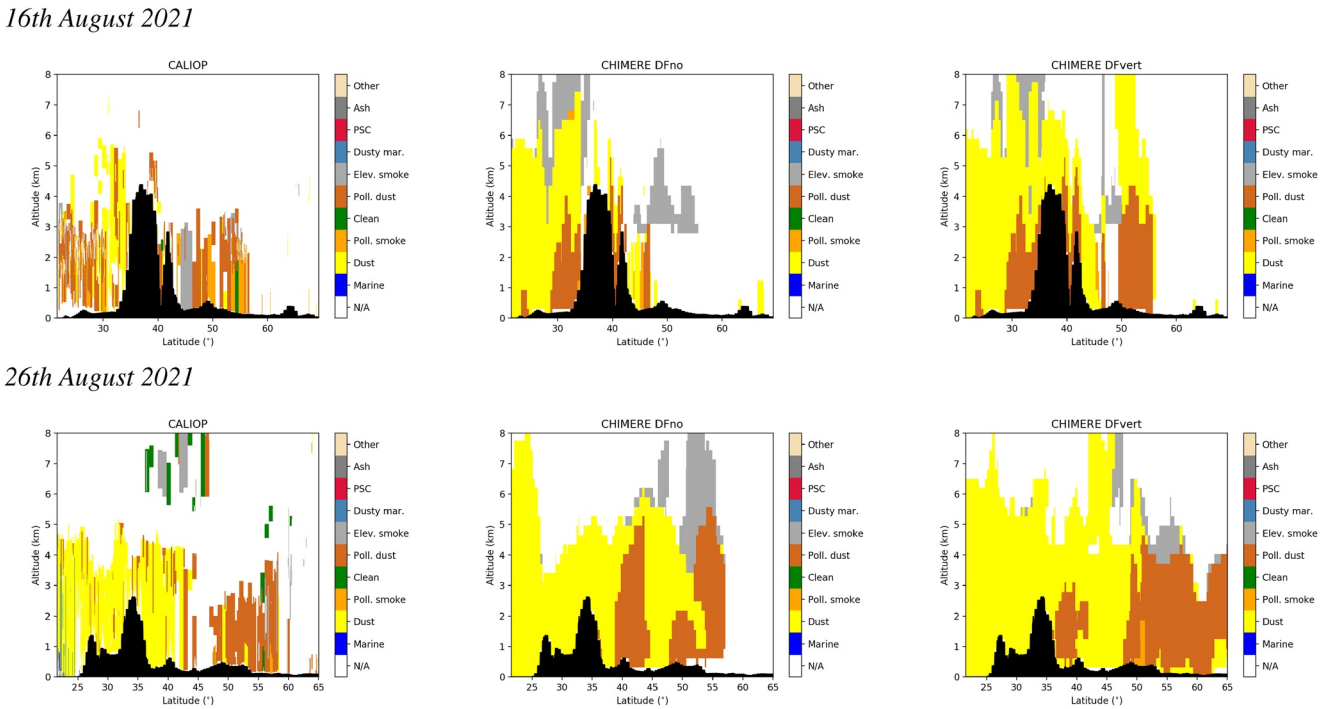


Figure 14. Comparison of vertical transects measured by the CALIOP lidar aboard CALIPSO and the two CHIMERE simulations DFno and DFvert, for the 16 August 2021, 08:40 UTC and 26 August 2021, 22:23 UTC.

important differences are in the North and East of the domain and they may be positive or negative, even if the most important values are positive, with ≈+3.75 ppb.

The patchy structure of ozone difference map is an effect of the model's coupling. Small changes on mineral dust emissions induce changes in mineral dust concentrations, then radiative effects, then photochemistry, then meteorology and pollutants concentrations such as ozone. These perturbations are then transported and the final picture mainly showing that taking direct and indirect effects into account in the model induces many interactions between processes difficult to prioritize and quantify.

A vertical cross-section of ozone is presented in Figure 17. The differences may be negative or positive from the surface to the top of the domain (8,000 m AGL). In the troposphere, differences are ≈± 2 ppb. These transects show that the changes in mineral dust are limited to close to the lower atmosphere, but changes for ozone are in the whole atmosphere and may be long-range transported.

Maps of differences are also presented for 2 m temperature and 10 m wind speed, Figure 18. It is noticeable that the increase in 2 m temperature is collocated to the additional mineral dust emissions. The changes are ±1K over the whole domain. Some changes are also noted for the 10 m wind speed with maximum changes of ±0.75 $m.s^{-1}$. These changes are in different places than the mineral dust emissions and ozone changes mainly show a non-linear effect, transported in the modeled domain.

4.4. Correlation

With these time-series, the question becomes to quantify the impact of this new process on the correlation between observations and model. The model performances show a large variability of spatial correlation depending on the parameter. But, mainly, adding the interaction between fires and dust is not always an important gain in the correlation comparisons. That is why a scatter-plot as presented in Figure 19 is more relevant to present the correlation coefficient results.

For O_3, $PM_{2.5}$ and AOD, the correlation ranges between 0 and 1. There is no simulation with a systematically better correlation. But a non-negligible variability is observed, showing that depending on the station, the correlation

21698996, 2022, 24, Downloaded from https://agupubs.onlinelibrary.wiley.com/doi/10.1029/2022JD037395 by Ecole Polytechnique, Wiley Online Library on [16/12/2022]. See the Terms and Conditions (https://onlinelibrary.wiley.com/terms-and-conditions) on Wiley Online Library for rules of use; OA articles are governed by the applicable Creative Commons License

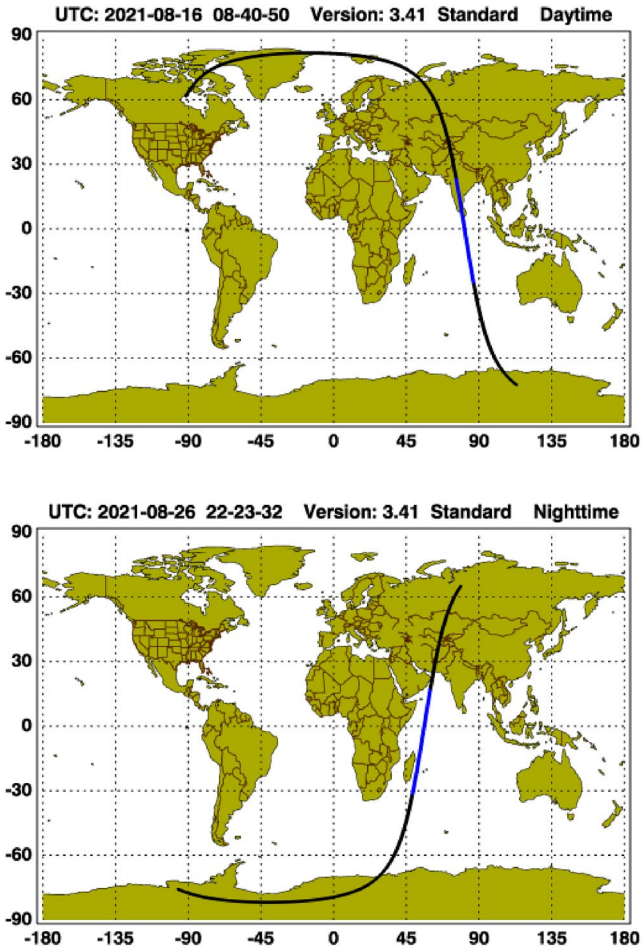


Figure 15. The two studied transects of the CALIPSO satellite for the 16 August 2021, 08:40 UTC and 26 August 2021, 22:23 UTC. Original images from the NASA web site: https://www-calipso.larc.nasa.gov/products/lidar.

may be better or not with DFvert. Even if the DFvert simulation represents a more realistic modeling (by adding a realistic process), there is no major impact on the surface concentrations (O_3, $PM_{2.5}$) or the aerosols atmospheric load (through the AOD).

Figure 20 presents maps of differences of statistical scores calculated for ozone and using the EEA measurements. These EEA measurements are located in western Europe only. The differences between DFvert and DFno show a decrease in scores with blue colors and an increase with red colors. For the correlation, the overall differences are low, between −0.015 and 0.015. Differences alternate between negative and positive values and it is difficult to have a region with a systematic response. The same behavior is noted for the bias. The bias changes between −0.375 and 0.375 ppb. The values are also very low, even if they are in average. But by comparing the two, correlation and bias differences, it appears that where the bias decreases, the correlation increase, like over the Belgium and Netherlands, showing a positive impact of the process.

4.5. Aerosol Size Distribution

In this section, we compare the aerosol size distributions between AERONET and the model. All modeled aerosol species are cumulated in each model bin to have a total aerosol concentration per size. The model has 10 bins when the AERONET product has 15 bins. Results are presented, in Figure 21, for stations with available data and close as possible of the wildfires regions. Unfortunately, the closest stations of the additional dust emissions did not provide such data. Stations with data are here Athens (Greece), Lampedusa (Italia) and IASBS (Iran). Clearly, the modeling of the aerosol size distribution remains a challenge and it is true for all chemistry-transport models (Seinfeld & Pandis, 2006). With observations, we can see two distinct modes, one peaking around the mean mass median diameter $D_p \approx 0.2$ µm and the second one around $D_p \approx 3$ µm.

Overall, results are not very stable and the modeled size distribution varies a lot compared to the observations: one time DFno provides better results, one time it is DFvert. In Athens, for the 28 August 15:00 UTC, the modeled fine mode is too little compared to the AERONET value. The coarse mode is better modeled with DFno than with DFvert. But for the 30 August, the result is the opposite: the coarse mode is better modeled with DFvert. In IASBS, the fine mode is underestimated for the 2 days. A common point is that the coarse mode is closer to the observations with DFvert than with DFno. In Lampedusa, the coarse mode dominates in the observations. The model is able to reproduce this and the comparison is better with DFno for the 28 August but better with DFvert for 30 August. Finally, there is no clear benefit to have the additional mineral dust emissions for the size distribution: results are different between DFno and DFvert but there is no systematic gain compared to observations.

A complementary way to understand the changes in aerosol size distribution is to split the aerosol individual contributions. It is presented in Figure 22 corresponding to the 28 August 2021 12:00 UTC at the station IASBS. When the fine mode shows low concentrations, its composition is made up of different species. It is different for the coarse mode when the composition is mainly made up of mineral dust. The increase is a direct impact of the additional emissions due to fires. The magnitude is realistic, showing that the parameterization used is in the correct order of magnitude.

4.6. Sensitivity Tests

The hypotheses done are numerous and some of them can be evaluated using sensitivity tests. In this section, two tests are performed, corresponding to sensitive parameters. They are done on what we consider to be the most uncertain and/or sensitive terms in the new parameterization. But other weak points exist. The first sensitivity test

21698996, 2022, 24, Downloaded from https://agupubs.onlinelibrary.wiley.com/doi/10.1029/2022JD037395 by Ecole Polytechnique, Wiley Online Library on [16/12/2022]. See the Terms and Conditions (https://onlinelibrary.wiley.com/terms-and-conditions) on Wiley Online Library for rules of use; OA articles are governed by the applicable Creative Commons License

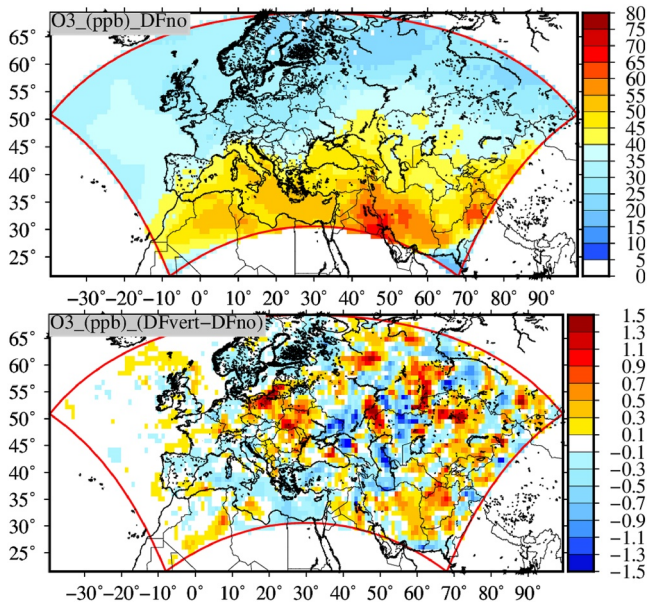


Figure 16. Surface concentrations maps of ozone (ppb). Values are for the DFno simulation (left) and the differences between DFno and DFvert. Values are time-averaged over the period 15–31 August 2021.

is on the magnitude of the possible increase of wind speed. The second one is the using the model online, with a feedback from aerosols to meteorology, in place of the offline version.

Numerous other sensitivity tests are possible: for example, the soil type considered as newly erodible, the roughness length value or the percentage of surface newly erodible. Some of these parameters were tested and the results showed that the impact was very small. The main reason is that the surfaces affected by fires are less important that the ones already considered as erodible without fires. This is true over Europe (where there is at the same time fires and erodible soils), but will be more over Africa or Australia for example, As pointed out by Mandel et al. (2011), the fires induce non negligible additional sensible and latent heat fluxes that have to be added in the surface flux budget in the meteorological model. By changing surface fluxes, pyroconvection also modifies the precipitation regimes downwind large fires, then also mineral dust wet deposition (Zhang et al., 2019). Another uncertainty is not taking the fire type and the burning vegetation type into account when it comes to the intensity of the mineral dust local emissions. This aspect could be a promising future development and improvement. But now, there is no available informations capable of providing constraints for this type of calculation. For analysis or forecast, the fires input data used in this study, the CAMS product, does not contain information about these types of data. And even if the information exists, there is no data/study able to quantify the amount of dust emission as a function of the fire or vegetation type.

4.6.1. The Magnitude of the Potential Wind Speed Change

One fixed parameter is the value of the wind increase as a function of the burnt area surface. All results were presented with a value of $|U|_{max} = u_c = 3$ m s^{-1} in Equation 5. This corresponds for the test to "DFvert" in Figure 23. In addition, the two months period was resimulated with $u_c = 5$ m s^{-1}, corresponding to DFvert5. The time-series presented are for AOD and for the Dushanbe site, close to the additional emissions, and for the whole modeled period, from 1 July to 31 August 2021. Modeled results are compared to the AERONET measurements (as in Figure 11). The differences between the two models configurations appears only at the end of the period: from 10 to 31 August. The difference values are not very important and show that the results are not very sensitive to the value of $|U|_{max}$. Even if this parameter is difficult to constrain, it is hopefully not a blocking point in the use of this parameterization.

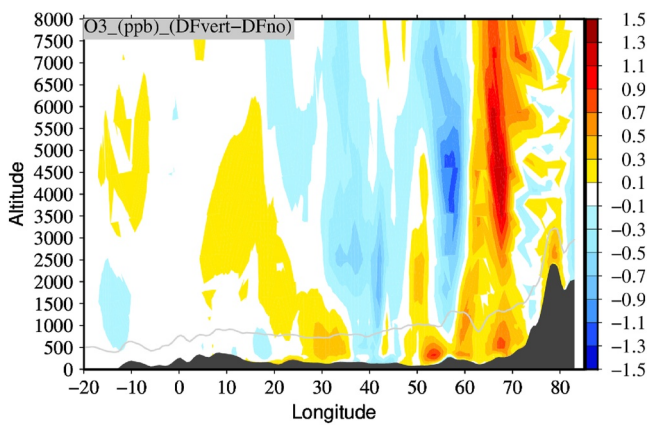


Figure 17. Vertical cross-sections of ozone concentrations as differences DFvert minus DFno. Values are time-averaged for latitudes between 35° and 45°W and for the period 15–31 August 2021.

4.6.2. Feedback of Aerosols on Meteorology

The analysis of the previous results showed that the additional mineral dust emission induces a lot of changes in the atmospheric composition: meteorological variables are different as well as all atmospheric concentrations of gaseous and aerosol species. It is then interesting to know if the impact on mineral dust is mainly due to its additional emissions or too many interactions between meteorology and aerosol content. In offline models, commonly used for analysis and forecast, the impact of aerosol concentrations is limited to photolytic chemistry (if taken into account in the chemistry-transport model), with then no retroaction from aerosol to meteorology. Thus, adding new emissions generally induces an increase of concentrations of the emitted species, and on other species impacted by chemical reactions. The offline model version makes possible the calculation of ozone change and to compare it to the results in Figure 16. Results are presented in Figure 24 and show very little changes in ozone surface concentrations (note that the color scale was changed to fit the low difference values). In offline mode, the impact on ozone reaches only ≈± 0.5 ppb. In online mode, the change was

21698996, 2022, 24, Downloaded from https://agupubs.onlinelibrary.wiley.com/doi/10.1029/2022JD037395 by Ecole Polytechnique, Wiley Online Library on [16/12/2022]. See the Terms and Conditions (https://onlinelibrary.wiley.com/terms-and-conditions) on Wiley Online Library for rules of use; OA articles are governed by the applicable Creative Commons License

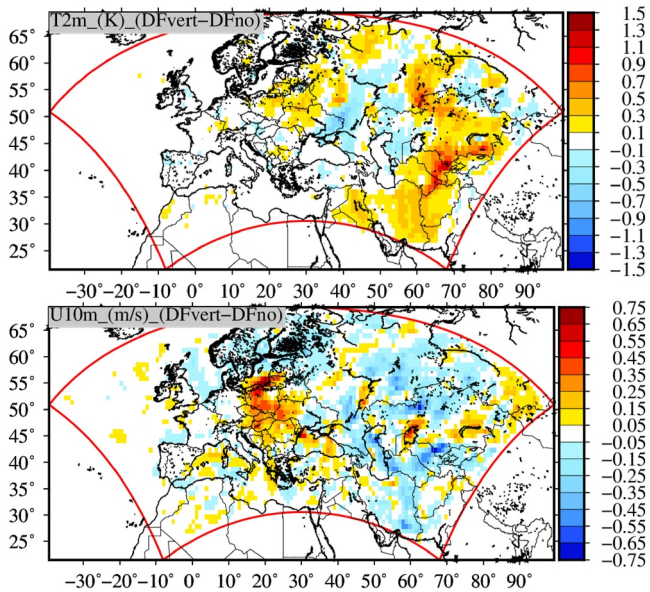


Figure 18. Surface maps of differences between DFno and DFvert for the 2 m temperature (K) and the 10 m wind speed ($m \cdot s^{-1}$). Values are time-averaged over the period 15–31 August 2021.

larger and rises to ≈± 5 ppb. It means that the most important impact is not due to a change of photochemical chemistry but to changes in meteorology mainly temperature and water vapor content (water vapor drives the radiative budget particularly at night), with then retroactions through indirect effects on chemistry (Bessagnet et al., 2020). It is surprising and questioning to observe such large effects despite the activation of nudging that is supposed to constraint the simulation and confirms some recent findings (He et al., 2017) where they show significant impact of this kind of aerosol feedbacks on ground temperatures.

5. Conclusion

The main goal of this study was to implement the sub-grid scale effect of wildfire outbreaks on mineral dust co-emissions. These additional emissions may be induced by mainly two processes: (a) a horizontal convergence of the near-surface wind speed due to the horizontal gradient in temperature between the fires and its surrounding, (b) the pyroconvection increasing turbulence in the fire column and entraining aerosol from the surface. This process was already studied but at very local scale. In this study, we try to implement this process in a regional chemistry-transport model, by adding a new sub-grid scale process. To take into account this process, we have to consider two time scales: (a) a change in the soil and surface characteristics: this may appear during and after the fire and remains for several months or years depending on the biome, (b) during the fire, a change in the wind speed, at the origin of mineral dust emissions. The quantification of this impact remains uncertain and numerous hypothesis are made to make this calculation possible. These hypotheses are realistic compared to the existing literature, even if measurements adapted to the situation are missing.

To quantify the impact of wildfires on mineral dust emissions, two months in summer 2021 were simulated over Europe and Asia with the models WRF and CHIMERE. The CHIMERE model used is the latest model version (v2020r3) in its online mode. The main model developments are done in CHIMERE, while WRF was not modified. In case of an active fire detection using MODIS data, the soil moisture becomes 0.1 kg kg^{-1}, the aeolian roughness length becomes $z_0 = 0.01$ cm and the soil becomes sand to have the same properties as erodible materials. These changes are only valid during the fire event. In addition, the erodibility is considered to be 100% for the burnt fraction area and this information is saved for the simulation for the following months. Only for the calculation of the mineral dust emissions, the 10 m wind speed is increased during a fire event. The increase follows a simple equation, linking the Fire Radiative Power range to an additional wind speed range. A test showed that results are not really sensitive to the value of the maximum possible wind speed increase. Finally, an important change is that the mineral dust emission, depending on the fire and atmospheric properties, may be injected in the whole troposphere whereas it is injected only at the surface in current models.

The first expected impact of additional mineral dust emissions is on its own concentrations. The interest of the new scheme is to have new locations emitting dust, not a priori listed in the used inventories. In this study, we expected to increase the correlation coefficient between measured and modeled AOD, but it was not systematically the case. It shows that the addition of a location is not the only uncertainty on dust modeling and that transport and deposition also have an important role in the atmospheric mineral dust life cycle. The second expected impact is on the other pollutants through the reduction of photolysis and other direct and indirect effects. This impact appears to be significant since, in time averaged during 15 days, ozone may change by ≈± 3 ppb over some locations. The 2 m temperature is also modified on average by ≈± 1 K. This effect does not appear if the model is used offline (only photolysis is impacted by a change on aerosol) meaning that the impact on the meteorology is important with this process.

21698996, 2022, 24, Downloaded from https://agupubs.onlinelibrary.wiley.com/doi/10.1029/2022JD037395 by Ecole Polytechnique, Wiley Online Library on [16/12/2022]. See the Terms and Conditions (https://onlinelibrary.wiley.com/terms-and-conditions) on Wiley Online Library for rules of use; OA articles are governed by the applicable Creative Commons License

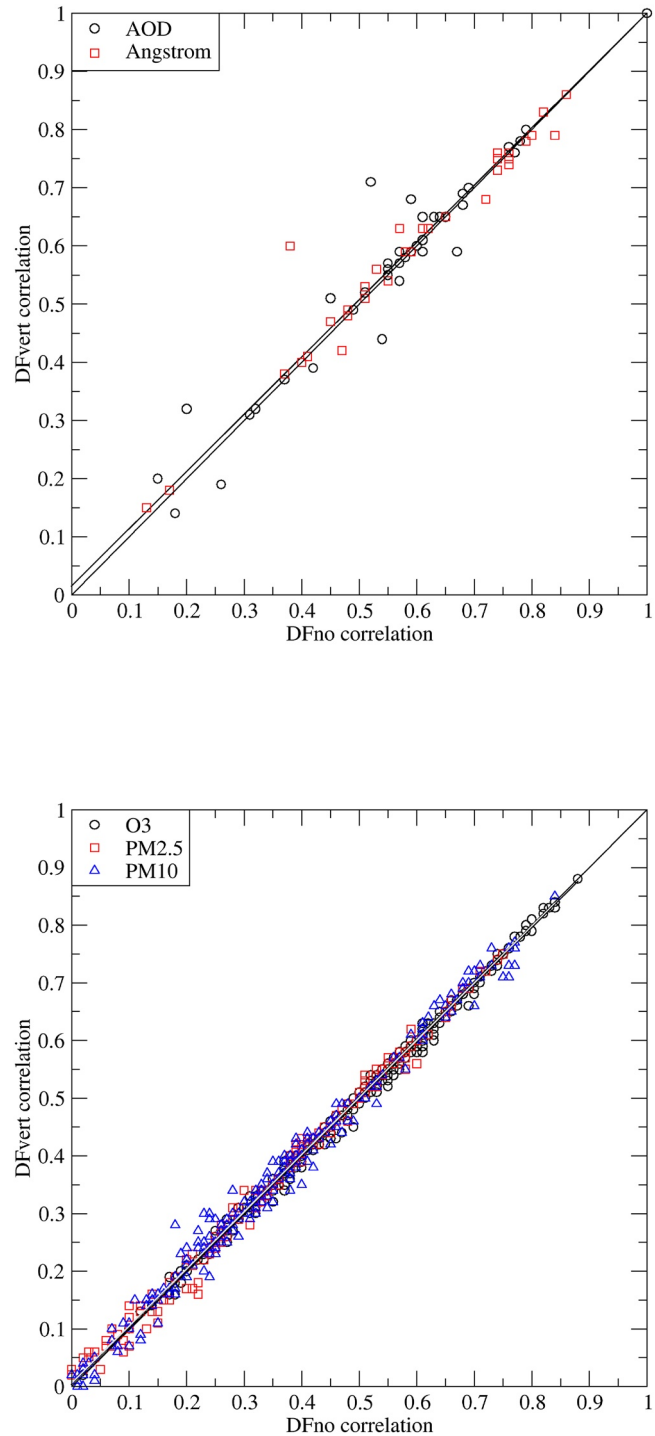


Figure 19. Scatter-plot of correlation calculated for the two simulations, DFno and DFvert, and between observations and model results for (a) O_3, $PM_{2.5}$ and PM_{10} and (b) AOD and Angström exponent. Values are for the period from 1 July to 31 August 2021. Measurements used are those of the stations presented in Figure 8.

21698996, 2022, 24, Downloaded from https://agupubs.onlinelibrary.wiley.com/doi/10.1029/2022JD037395 by Ecole Polytechnique, Wiley Online Library on [16/12/2022]. See the Terms and Conditions (https://onlinelibrary.wiley.com/terms-and-conditions) on Wiley Online Library for rules of use; OA articles are governed by the applicable Creative Commons License

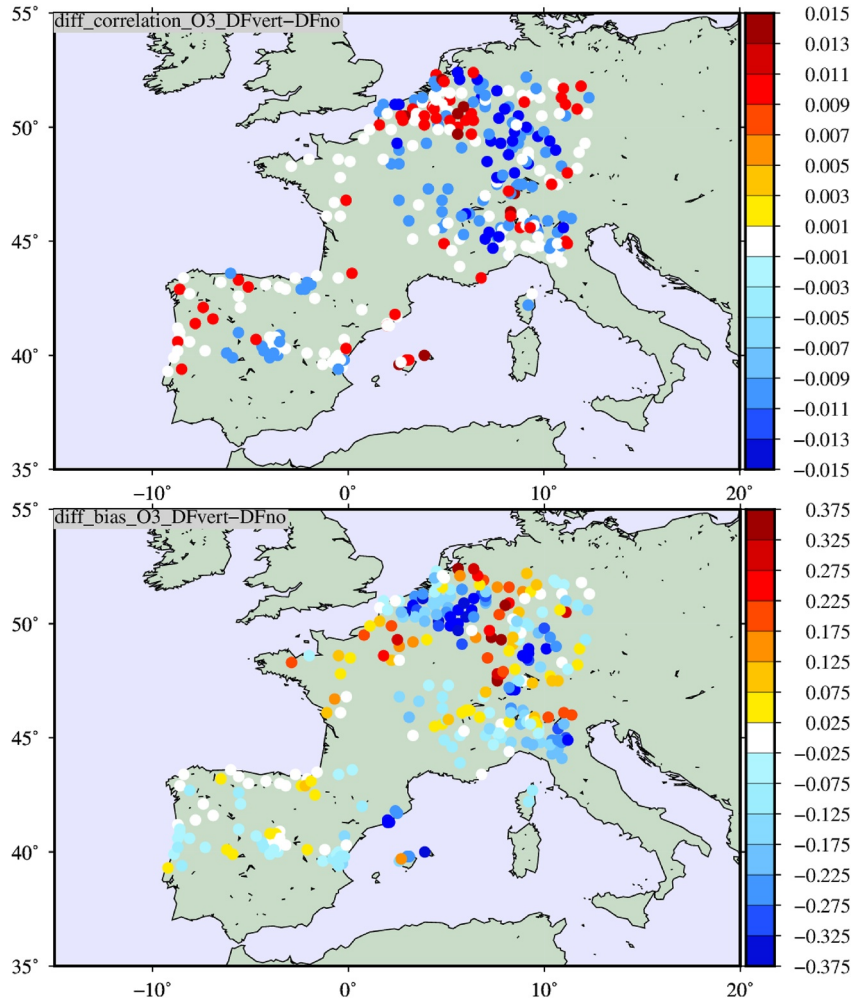


Figure 20. Maps of correlation and bias differences for ozone and for the simulations DFvert and DFno.

21698996, 2022, 24, Downloaded from https://agupubs.onlinelibrary.wiley.com/doi/10.1029/2022JD037395 by Ecole Polytechnique, Wiley Online Library on [16/12/2022]. See the Terms and Conditions (https://onlinelibrary.wiley.com/terms-and-conditions) on Wiley Online Library for rules of use; OA articles are governed by the applicable Creative Commons License

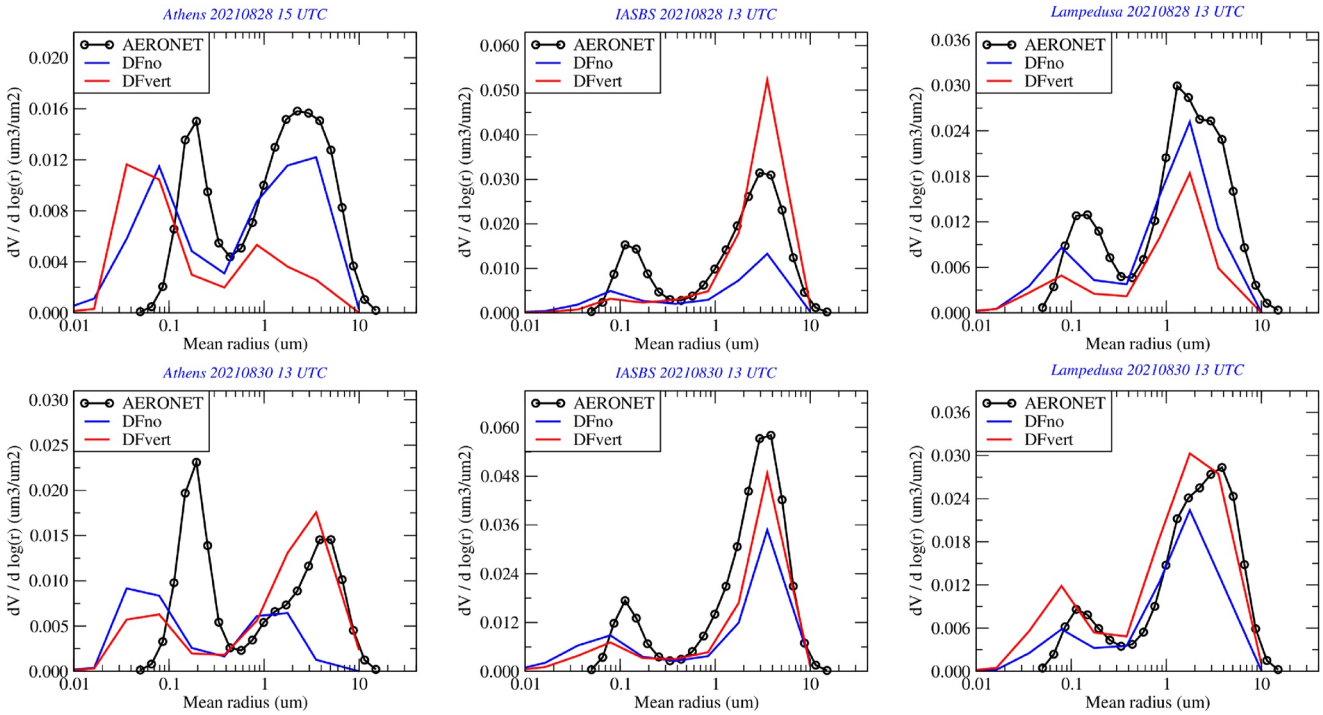


Figure 21. Aerosol size distribution measured by AERONET (inversion product) and calculated with CHIMERE for the two simulations DFno and DFvert. Comparison is performed for the sites of Athens, IASBS and Lampedusa, and for the 28 and 30 August 2021.

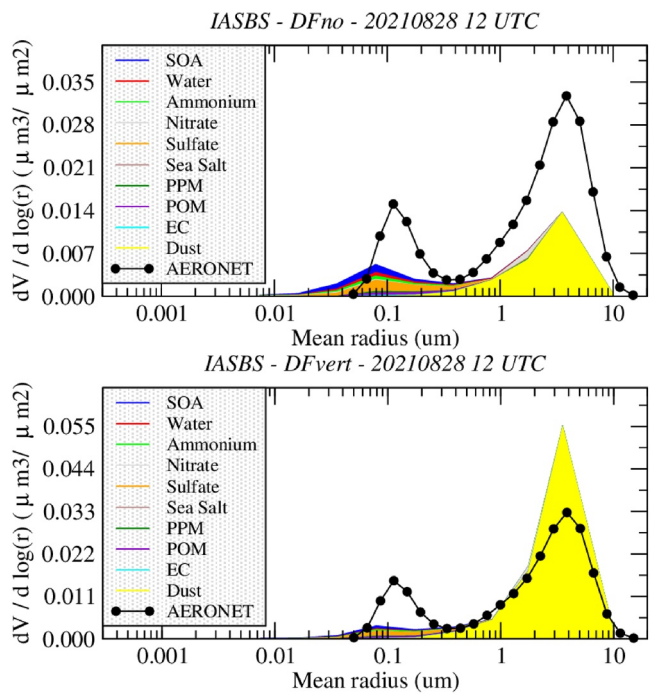


Figure 22. Aerosol size distribution, with the aerosol composition, at IASBS for the 28 August 2021 12:00 UTC and for the DFvert simulation.

21698996, 2022, 24, Downloaded from https://agupubs.onlinelibrary.wiley.com/doi/10.1029/2022JD037395 by Ecole Polytechnique, Wiley Online Library on [16/12/2022]. See the Terms and Conditions (https://onlinelibrary.wiley.com/terms-and-conditions) on Wiley Online Library for rules of use; OA articles are governed by the applicable Creative Commons License

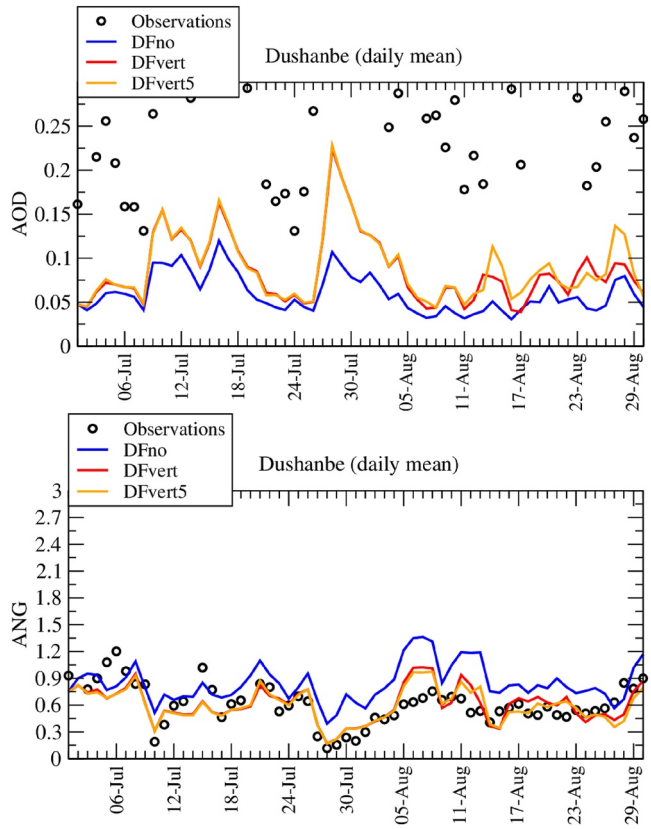


Figure 23. Time-series of AOD and Angström component at the Dushanbe AERONET station and for the AERONET observations and two simulations involving the impact of fires on dust emissions, but with the maximum possible wind speed of $|U| = 3$ m s^{-1} (DFvert configuration) and the sensitivity test with $|U| = 5$ m s^{-1} (DFvert5 configuration).

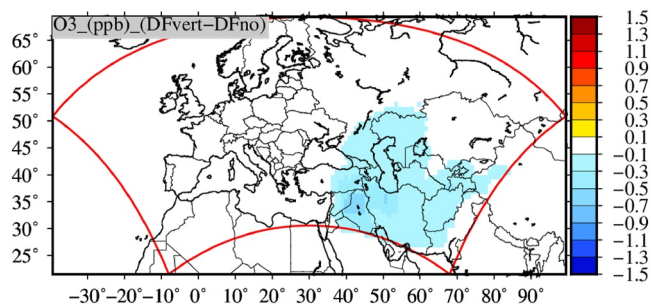


Figure 24. Surface concentration maps of ozone (ppb) and differences DFvert minus DFno. Simulations are performed without direct and indirect effects: the CHIMERE model reads WRF files but there is no retroaction from CHIMERE to WRF. Values are averaged over the period 15–31 August 2021.

Conflict of Interest

The authors declare no conflicts of interest relevant to this study.

Data Availability Statement

The simulations were performed using the WRF model v3.7.1 (Powers et al., 2017), and the CHIMERE chemistry-transport model (Menut et al., 2021).

21698996, 2022, 24, Downloaded from https://agupubs.onlinelibrary.wiley.com/doi/10.1029/2022JD037395 by Ecole Polytechnique, Wiley Online Library on [16/12/2022]. See the Terms and Conditions (https://onlinelibrary.wiley.com/terms-and-conditions) on Wiley Online Library for rules of use; OA articles are governed by the applicable Creative Commons License

Acknowledgments
The authors acknowledge the OASIS modeling team for their support with the OASIS coupler, the WRF developers team for the free use of their model. We thank the investigators and staff who maintain and provide the AERONET data (https://aeronet.gsfc.nasa.gov/). European Environmental Agency (EEA) is acknowledged for their air quality station data that is provided and freely downloadable (https://www.eea.europa.eu/data-and-maps/data/aqereporting-8).

References

Alfaro, S. C., & Gomes, L. (2001). Modeling mineral aerosol production by wind erosion: Emission intensities and aerosol size distribution in source areas. *Journal of Geophysical Research*, *106*(D16), 18075–18084. https://doi.org/10.1029/2000jd900339

Beegum, S., Gherboudj, I., Chaouch, N., Couvidat, F., Menut, L., & Ghedira, H. (2016). Simulating aerosols over Arabian Peninsula with CHIMERE: Sensitivity to soil, surface parameters and anthropogenic emission inventories. *Atmospheric Environment*, *128*, 185–197. https://doi.org/10.1016/j.atmosenv.2016.01.010

Bessagnet, B., Menut, L., Aymoz, G., Chepfer, H., & Vautard, R. (2008). Modelling dust emissions and transport within Europe: The Ukraine March 2007 event. *Journal of Geophysical Research*, *113*(D15), D15202. https://doi.org/10.1029/2007JD009541

Bessagnet, B., Menut, L., Lapere, R., Couvidat, F., Jaffrezo, J.-L., Mailler, S., et al. (2020). High resolution chemistry transport modeling with the on-line CHIMERE-WRF model over the French Alps-analysis of a feedback of surface particulate matter concentrations on mountainous meteorology. *Atmosphere*, *11*(6), 565. https://doi.org/10.3390/atmos11060565

Briant, R., Tuccella, P., Deroubaix, A., Khvorostyanov, D., Menut, L., Mailler, S., & Turquety, S. (2017). Aerosol–radiation interaction modelling using online coupling between the WRF 3.7.1 meteorological model and the CHIMERE 2016 chemistry-transport model, through the OASIS3-MCT coupler. *Geoscientific Model Development*, *10*(2), 927–944. https://doi.org/10.5194/gmd-10-927-2017

Burton, S. P., Hair, J. W., Kahnert, M., Ferrare, R. A., Hostetler, C. A., Cook, A. L., et al. (2015). Observations of the spectral dependence of linear particle depolarization ratio of aerosols using NASA Langley airborne High Spectral Resolution Lidar. *Atmospheric Chemistry and Physics*, *15*(23), 13453–13473. https://doi.org/10.5194/acp-15-13453-2015

Carslaw, K. S., Boucher, O., Spracklen, D. V., Mann, G. W., Rae, J. G. L., Woodward, S., & Kulmala, M. (2010). A review of natural aerosol interactions and feedbacks within the Earth system. *Atmospheric Chemistry and Physics*, *10*(4), 1701–1737. https://doi.org/10.5194/acp-10-1701-2010

Cowie, S. M., Marsham, J. H., & Knippertz, P. (2015). The importance of rare, high-wind events for dust uplift in northern Africa. *Geophysical Research Letters*, *42*(19), 8208–8215. https://doi.org/10.1002/2015GL065819

Dong, X., Fu, J. S., Huang, K., Lin, N.-H., Wang, S.-H., & Yang, C.-E. (2018). Analysis of the Co-existence of long-range transport biomass burning and dust in the subtropical West Pacific Region. *Nature Scientific Reports*, *8962*(1), 2045–2322. https://doi.org/10.1038/s41598-018-27129-2

Dubovik, O., & King, M. D. (2000). A flexible inversion algorithm for retrieval of aerosol optical properties from sun and sky radiance measurements. *Journal of Geophysical Research*, *105*(D16), 20673–20696. https://doi.org/10.1029/2000JD900282

Foroutan, H., & Pleim, J. E. (2017). Improving the simulation of convective dust storms in regional-to-global models. *Journal of Advances in Modeling Earth Systems*, *9*(5), 2046–2060. https://doi.org/10.1002/2017MS000953

Gonzi, S., Palmer, P. I., Paugam, R., Wooster, M., & Deeter, M. N. (2015). Quantifying pyroconvective injection heights using observations of fire energy: Sensitivity of spaceborne observations of carbon monoxide. *Atmospheric Chemistry and Physics*, *15*(8), 4339–4355. https://doi.org/10.5194/acp-15-4339-2015

He, J., Glotfelty, T., Yahya, K., Alapaty, K., & Yu, S. (2017). Does temperature nudging overwhelm aerosol radiative effects in regional integrated climate models? *Atmospheric Environment*, *154*, 42–52. https://doi.org/10.1016/j.atmosenv.2017.01.040

Hodnebrog, O., Solberg, S., Stordal, F., Svendby, T., Simpson, D., Gauss, M., et al. (2012). Impact of forest fires, biogenic emissions and high temperatures on the elevated Eastern Mediterranean ozone levels during the hot summer of 2007. *Atmospheric Chemistry and Physics*, *12*(18), 8727–8750. https://doi.org/10.5194/acp-12-8727-2012

Holben, B., Tanre, D., Smirnov, A., Eck, T. F., Slutsker, I., Abuhassan, N., et al. (2001). An emerging ground-based aerosol climatology: Aerosol optical depth from AERONET. *Journal of Geophysical Research*, *106*(D11), 12067–12097. https://doi.org/10.1029/2001jd900014

Jenkin, M., & Clemitshaw, K. (2000). Ozone and other secondary photochemical pollutants: Chemical processes governing their formation in the planetary boundary layer. *Atmospheric Environment*, *34*(16), 2499–2527. https://doi.org/10.1029/2019GL084534

Kaiser, J. W., Heil, A., Andreae, M. O., Benedetti, A., Chubarova, N., Jones, L., et al. (2012). Biomass burning emissions estimated with a global fire assimilation system based on observed fire radiative power. *Biogeosciences*, *9*(1), 527–554. https://doi.org/10.5194/bg-9-527-2012

Klose, M., & Shao, Y. (2012). Stochastic parameterization of dust emission and application to convective atmospheric conditions. *Atmospheric Chemistry and Physics*, *12*(16), 7309–7320. https://doi.org/10.5194/acp-12-7309-2012

Klose, M., Shao, Y., Li, X., Zhang, H., Ishizuka, M., Mikami, M., & Leys, J. F. (2014). Further development of a parameterization for convective turbulent dust emission and evaluation based on field observations. *Journal of Geophysical Research*, *119*(17), 10441–10457. https://doi.org/10.1002/2014JD021688

Konovalov, I. B., Beekmann, M., Berezin, E. V., Petetin, H., Mielonen, T., Kuznetsova, I. N., & Andreae, M. O. (2015). The role of semi-volatile organic compounds in the mesoscale evolution of biomass burning aerosol: A modeling case study of the 2010 mega-fire event in Russia. *Atmospheric Chemistry and Physics*, *15*(23), 13269–13297. https://doi.org/10.5194/acp-15-13269-2015

Konovalov, I. B., Beekmann, M., Kuznetsova, I. N., Yurova, A., & Zvyagintsev, A. M. (2011). Atmospheric impacts of the 2010 Russian wildfires: Integrating modelling and measurements of an extreme air pollution episode in the Moscow region. *Atmospheric Chemistry and Physics*, *11*(19), 10031–10056. https://doi.org/10.5194/acp-11-10031-2011

Lareau, N. P., & Clements, C. B. (2015). Cold smoke: Smoke-induced density currents cause unexpected smoke transport near large wildfires. *Atmospheric Chemistry and Physics*, *15*(20), 11513–11520. https://doi.org/10.5194/acp-15-11513-2015

Laurent, P., Mouillot, F., Moreno, M. V., Yue, C., & Ciais, P. (2019). Varying relationships between fire radiative power and fire size at a global scale. *Biogeosciences*, *16*(2), 275–288. https://doi.org/10.5194/bg-16-275-2019

Mailler, S., Menut, L., di Sarra, A. G., Becagli, S., Di Iorio, T., Bessagnet, B., et al. (2016). On the radiative impact of aerosols on photolysis rates: Comparison of simulations and observations in the lampedusa island during the ChArMEx/ADRIMED campaign. *Atmospheric Chemistry and Physics*, *16*(3), 1219–1244. https://doi.org/10.5194/acp-16-1219-2016

Mandel, J., Beezley, J. D., & Kochanski, A. K. (2011). Coupled atmosphere-wildland fire modeling with WRF 3.3 and SFIRE 2011. *Geoscientific Model Development*, *4*(3), 591–610. https://doi.org/10.5194/gmd-4-591-2011

Menut, L. (2018). Modeling of mineral dust emissions with a Weibull wind speed distribution including subgrid-scale orography variance. *Journal of Atmospheric and Oceanic Technology*, *35*(6), 1221–1236. https://doi.org/10.1175/JTECH-D-17-0173.1

Menut, L., Bessagnet, B., Briant, R., Cholakian, A., Couvidat, F., Mailler, S., et al. (2021). The CHIMERE v2020r1 online chemistry-transport model [Software]. Geoscientific Model Development, *14*(11), 6781–6811. https://doi.org/10.5194/gmd-14-6781-2021

Menut, L., Flamant, C., Turquety, S., Deroubaix, A., Chazette, P., & Meynadier, R. (2018). Impact of biomass burning on pollutant surface concentrations in megacities of the Gulf of Guinea. *Atmospheric Chemistry and Physics*, *18*(4), 2687–2707. https://doi.org/10.5194/acp-18-2687-2018

Menut, L., Perez Garcia-Pando, C., Haustein, K., Bessagnet, B., Prigent, C., & Alfaro, S. (2013). Relative impact of roughness and soil texture on mineral dust emission fluxes modeling. *Journal of Geophysical Research*, *118*(12), 6505–6520. https://doi.org/10.1002/jgrd.50313

21698996, 2022, 24, Downloaded from https://agupubs.onlinelibrary.wiley.com/doi/10.1029/2022JD037395 by Ecole Polytechnique, Wiley Online Library on [16/12/2022]. See the Terms and Conditions (https://onlinelibrary.wiley.com/terms-and-conditions) on Wiley Online Library for rules of use; OA articles are governed by the applicable Creative Commons License

Menut, L., Schmechtig, C., & Marticorena, B. (2005). Sensitivity of the sandblasting fluxes calculations to the soil size distribution accuracy. *Journal of Atmospheric and Oceanic Technology*, *22*(12), 1875–1884. https://doi.org/10.1175/jtech1825.1

Morman, S. A., & Plumlee, G. S. (2013). The role of airborne mineral dusts in human disease. *Aeolian Research*, *9*, 203–212. https://doi.org/10.1016/j.aeolia.2012.12.001

Omar, A., Winker, D. M., Vaughan, M. A., Hu, Y., Trepte, C. R., Ferrare, R. A., et al. (2010). The CALIPSO automated aerosol classification and lidar ratio selection algorithm. *Journal of Atmospheric and Oceanic Technology*, *26*(10), 1994–2014. https://doi.org/10.1175/2009jtecha1231.1

Péré, J. C., Bessagnet, B., Pont, V., Mallet, M., & Minvielle, F. (2015). Influence of the aerosol solar extinction on photochemistry during the 2010 Russian wildfires episode. *Atmospheric Chemistry and Physics*, *15*(19), 10983–10998. https://doi.org/10.5194/acp-15-10983-2015

Powers, J. G., Klemp, J. B., Skamarock, W. C., Davis, C. A., Dudhia, J., Gill, D. O., et al. (2017). The Weather Research and forecasting model: Overview, system efforts, and future directions [Software]. Bulletin of the American Meteorological Society, *98*(8), 1717–1737. https://doi.org/10.1175/BAMS-D-15-00308.1

Rea, G., Turquety, S., Menut, L., Briant, R., Mailler, S., & Siour, G. (2015). Source contributions to 2012 summertime aerosols in the Euro-Mediterranean region. *Atmospheric Chemistry and Physics*, *15*(14), 8013–8036. https://doi.org/10.5194/acp-15-8013-2015

Rémy, S., Veira, A., Paugam, R., Sofiev, M., Kaiser, J. W., Marenco, F., et al. (2017). Two global data sets of daily fire emission injection heights since 2003. *Atmospheric Chemistry and Physics*, *17*(4), 2921–2942. https://doi.org/10.5194/acp-17-2921-2017

Roberts, A. J., Woodage, M. J., Marsham, J. H., Highwood, E. J., Ryder, C. L., McGinty, W., et al. (2018). Can explicit convection improve modelled dust in summertime West Africa? *Atmospheric Chemistry and Physics*, *18*(12), 9025–9048. https://doi.org/10.5194/acp-18-9025-2018

Schepanski, K. (2018). Transport of mineral dust and its impact on climate. *Geosciences*, *8*(5), 151. https://doi.org/10.3390/geosciences8050151

Schlosser, J. S., Braun, R. A., Bradley, T., Dadashazar, H., MacDonald, A. B., Aldhaif, A. A., et al. (2017). Analysis of aerosol composition data for western United States wildfires between 2005 and 2015: Dust emissions, chloride depletion, and most enhanced aerosol constituents. *Journal of Geophysical Research: Atmospheres*, *122*(16), 8951–8966. https://doi.org/10.1002/2017JD026547

Seinfeld, J., & Pandis, S. (2006). *Atmospheric chemistry and physics: From air pollution to climate change* (2nd ed.). Wiley-Interscience.

Sofiev, M., Ermakova, T., & Vankevich, R. (2012). Evaluation of the smoke-injection height from wild-land fires using remote-sensing data. *Atmospheric Chemistry and Physics*, *12*(4), 1995–2006. https://doi.org/10.5194/acp-12-1995-2012

Tesche, M., Wandinger, U., Ansmann, A., Althausen, D., Muller, D., & Omar, A. H. (2013). Ground-based validation of CALIPSO observations of dust and smoke in the Cape Verde region. *Journal of Geophysical Research: Atmospheres*, *118*(7), 2889–2902. https://doi.org/10.1002/jgrd.50248

Tuccella, P., Menut, L., Briant, R., Deroubaix, A., Khvorostyanov, D., Mailler, S., et al. (2019). Implementation of aerosol-cloud interaction within WRF-CHIMERE online coupled model: Evaluation and investigation of the indirect radiative effect from anthropogenic emission reduction on the Benelux Union. *Atmosphere*, *10*(20), 20. https://doi.org/10.3390/atmos10010020

Veira, A., Kloster, S., Wilkenskjeld, S., & Remy, S. (2015). Fire emission heights in the climate system – Part 1: Global plume height patterns simulated by ECHAM6-HAM2. *Atmospheric Chemistry and Physics*, *15*(13), 7155–7171. https://doi.org/10.5194/acp-15-7155-2015

Wagner, R., Jähn, M., & Schepanski, K. (2018). Wildfires as a source of airborne mineral dust – Revisiting a conceptual model using large-eddy simulation (LES). *Atmospheric Chemistry and Physics*, *18*(16), 11863–11884. https://doi.org/10.5194/acp-18-11863-2018

Wagner, R., Schepanski, K., & Klose, M. (2021). The dust emission potential of agricultural-like fires-theoretical estimates from two conceptually different dust emission parameterizations. *Journal of Geophysical Research: Atmospheres*, *126*(18), e2020JD034355. https://doi.org/10.1029/2020JD034355

Wang, Q., Gu, J., & Wang, X. (2020). The impact of Sahara dust on air quality and public health in European countries. *Atmospheric Environment*, *241*, 117771. https://doi.org/10.1016/j.atmosenv.2020.117771

Wild, O., Zhu, X., & Prather, J. (2000). Fast-J: Accurate simulation of the in- and below-cloud photolysis in tropospheric chemical models. *Journal of Atmospheric Chemistry*, *37*(3), 245–282. https://doi.org/10.1023/a:1006415919030

Winker, D., Pelon, J., Coakley, J. A., Jr., Ackerman, S. A., Charlson, R. J., Colarco, P. R., et al. (2010). The CALIPSO mission: A global 3D view of aerosols and clouds. *Bulletin of the American Meteorological Society*, *91*(9), 1211–1229. https://doi.org/10.1175/2010bams3009.1

Ye, X., Arab, P., Ahmadov, R., James, E., Grell, G. A., Pierce, B., et al. (2021). Evaluation and intercomparison of wildfire smoke forecasts from multiple modeling systems for the 2019 Williams Flats fire. *Atmospheric Chemistry and Physics*, *21*(18), 14427–14469. https://doi.org/10.5194/acp-21-14427-2021

Yue, C., Ciais, P., Cadule, P., Thonicke, K., Archibald, S., Poulter, B., et al. (2014). Modelling the role of fires in the terrestrial carbon balance by incorporating SPITFIRE into the global vegetation model ORCHIDEE - Part 1: Simulating historical global burned area and fire regimes. *Geoscientific Model Development*, *7*(6), 2747–2767. https://doi.org/10.5194/gmd-7-2747-2014

Zhang, Y., Fan, J., Logan, T., Li, Z., & Homeyer, C. R. (2019). Wildfire impact on environmental thermodynamics and severe convective storms. *Geophysical Research Letters*, *46*(16), 10082–10093. https://doi.org/10.1029/2019GL084534

21698996, 2022, 24, Downloaded from https://agupubs.onlinelibrary.wiley.com/doi/10.1029/2022JD037395 by Ecole Polytechnique, Wiley Online Library on [16/12/2022]. See the Terms and Conditions (https://onlinelibrary.wiley.com/terms-and-conditions) on Wiley Online Library for rules of use; OA articles are governed by the applicable Creative Commons License